A pdf modeling study of self-similar turbulent free shear flows

D. C. Haworth[a] and S. B. Pope
Sibley School of Mechanical and Aerospace Engineering, Cornell University, Ithaca, New York 14853

(Received 10 September 1986; accepted 23 December 1986)

A modeled transport equation for the joint probability density function (pdf) of the velocities and a scalar has been solved numerically for four self-similar turbulent free shear flows: the plane mixing layer, the plane wake, the plane jet, and the axisymmetric jet. In the pdf equation, convection is treated exactly but the effects of viscosity, molecular diffusion, and the fluctuating pressure gradient have to be modeled. Five different models are evaluated; four of these are based on the Langevin equation for the fluid particle velocities, and the fifth is a particle pair interaction model. In each case, a stochastic mixing model represents the effects of molecular diffusion, and conditional modeling is included to account for intermittency. The resulting modeled pdf equation is solved by a Monte Carlo method. Calculated spreading rates and profiles of the mean velocity and Reynolds stresses show generally good agreement with experimental data for three of the five velocity models. However, discrepancies between the calculated and measured intermittency factor profiles, in particular for the plane mixing layer, reveal weaknesses in the conditional modeling.

I. INTRODUCTION

The one-point statistics of four self-similar turbulent free shear flows have been calculated by modeling and solving a transport equation for the joint probability density function (pdf) of the Eulerian velocities $\mathbf{U}(\mathbf{x},t)$ and a conserved passive scalar $\Phi(\mathbf{x},t)$, a "velocity-composition" joint pdf. Three terms are modeled in the pdf equation. These terms represent the effects of viscous dissipation, the fluctuating pressure gradient, and molecular diffusion. All closure models are expressed in Lagrangian form as models for the behavior of fluid particles. Five models are evaluated for the particle velocities (i.e., for the viscosity and the fluctuating pressure gradient). One is the generalized Langevin equation developed by Haworth and Pope[1]; three of the others are simplified versions of this Langevin equation, and the fifth is the particle interaction model described in Ref. 2. A stochastic mixing model[3] accounts for molecular diffusion, and intermittency is incorporated explicitly using the conserved passive scalar approach of Kollmann and Janicka.[4] To complete the closure, the dissipation time scale is assumed to be uniform across each flow. The resulting conditionally modeled joint pdf transport equation is solved by a Monte Carlo method.[2,5]

Lundgren[6,7] was the first to apply the method of modeling and solving a pdf equation derived from the governing Eulerian conservation equations for the flow field as an approach to turbulence closures. The method has since been developed and refined by a number of workers.[8–10] A thorough introduction to the pdf method and the Monte Carlo solution method may be found in Ref. 2. References 11 through 18 contain modeling studies based on the solution of a velocity-composition joint pdf equation. The pdf approach offers two advantages over one-point turbulence closures based on moment equations (e.g., $k-\epsilon$ models or second-order closures[19–21]): first, the joint pdf contains more complete statistical information than does any finite number of moments; and second, any one-point processes such as convection, buoyancy, and reaction can be treated without approximation.[2] For the constant-density inert flows considered here, this means that convective transport is treated without the usual gradient diffusion assumption. In common with other one-point closures, however, the one-point joint pdf contains no information on the frequency or length scale of the turbulent fluctuations. Scale information has to be provided separately. This is usually done either by carrying an additional modeled equation for the mean dissipation rate of turbulent kinetic energy or by specifying the dissipation time scale directly; the latter approach is adopted here. An alternative treatment that is natural in the framework of the pdf method is described in the conclusion of this paper.

The primary purpose of this work is to evaluate the five particle velocity models, with particular emphasis on the generalized Langevin equation. The performance of the generalized Langevin model in homogeneous flows is quite encouraging,[1] and the next level of complexity is the self-similar free shear flow. We apply the models to four of these: the plane mixing layer, the plane wake, the plane jet, and the axisymmetric jet. The quantities of interest are the rates of spread, streamwise mean velocity profiles, and Reynolds stress profiles. Any one-point statistic of the velocity and scalar fields can in principle be extracted from the numerical solution, but it is appropriate to limit the discussion to those quantities that are most revealing and for which the most reliable experimental data are available.

A secondary goal is to assess the intermittency modeling, which is essentially the same as that introduced in Ref. 12, in a broader class of flows. Since the effects of intermittency are included, statistics conditional on the fluid being turbulent or nonturbulent can also be calculated. Again, our emphasis is on the velocity modeling, and since the present intermittency modeling is found to be inadequate, the only conditional quantity that is shown is the intermittency factor (Sec. III E). The scalar is included in the formulation only as

[a] Present address: Fluid Mechanics Department, General Motors Research Laboratories, Warren, Michigan 48090.

 0031-9171/87/041026-19$01.90

a means of distinguishing turbulent from nonturbulent fluid; no statistics of the scalar field or joint velocity-scalar statistics are presented.

We begin in the following section with an introduction to the flows to be modeled. For the jets, we consider only those issuing into stagnant surroundings; for the plane mixing layer, we concentrate on the case where the low-speed stream is stagnant. The necessary notation is introduced and the available experimental data are evaluated. Section III contains a discussion of the pdf equation and the closure models. The numerical solution technique is then described in Sec. IV. Two different types of Monte Carlo solution algorithms are used, one for the (asymptotically self-similar) plane wake and a different one for the other three (exactly self-similar) flows. Results of the model calculations are presented and compared with experimental data and with each other in Sec. V. The final section contains a summary and conclusions.

II. SELF-SIMILAR FREE SHEAR FLOWS

In this section, we describe the four flows to be modeled and review the experimental data for each. Notation is introduced that will be used in the remainder of the paper. The flows are sketched in Figs. 1–4.

A. Flow descriptions

All of the flows considered are thin turbulent free shear flows, or free turbulent boundary layers. These flows are characterized by being remote from walls ("free") and by having a single predominant flow direction, the streamwise direction ("boundary layer").[22–24] In addition, each of the flows has a direction of statistical homogeneity, and they are all statistically stationary. The streamwise direction is denoted by x, the cross-stream direction (in which gradients of mean quantities are important) by y, and the direction of statistical homogeneity by z. Corresponding velocity components are U, V, and W. For the three plane flows, x, y, and z are as shown in Figs. 1–3, while for the axisymmetric jet, $x = x'$, $y = r'$, and $z = \theta$ (Fig. 4). Means are denoted by angled brackets $\langle\ \rangle$, and the usual decomposition of velocities and scalars into mean and fluctuating components is made:

$$U(\mathbf{x},t) = \langle U(\mathbf{x},t)\rangle + u(\mathbf{x},t),$$
$$V(\mathbf{x},t) = \langle V(\mathbf{x},t)\rangle + v(\mathbf{x},t),$$
$$W(\mathbf{x},t) = \langle W(\mathbf{x},t)\rangle + w(\mathbf{x},t),$$

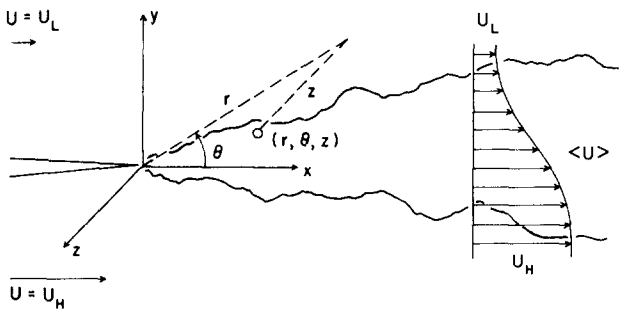

FIG. 1. The turbulent plane mixing layer.

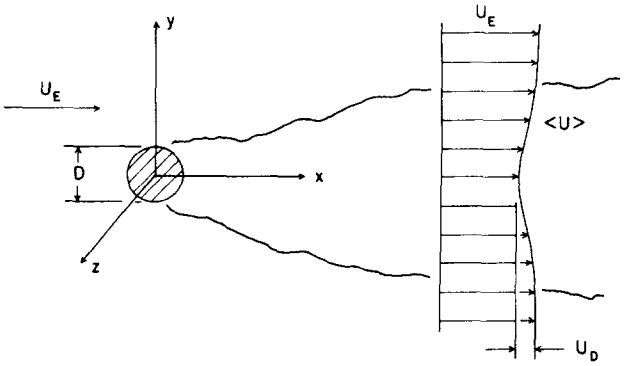

FIG. 2. The turbulent plane wake.

and

$$\Phi(\mathbf{x},t) = \langle \Phi(\mathbf{x},t)\rangle + \Phi'(\mathbf{x},t).$$

It is useful to define a characteristic velocity difference ΔU and width δ for each flow. For the plane mixing layer, we take ΔU to be the change in streamwise velocity across the flow, $\Delta U \equiv U_H - U_L$ (Fig. 1); for the plane wake, we take the centerline mean velocity deficit, $\Delta U \equiv U_D$ (Fig. 2); and, for the two jet flows, we take the centerline mean velocity $\Delta U \equiv U_C$ (Figs. 3 and 4). The length scale δ is defined in terms of the mean velocity profile $\langle U(y)\rangle$. We indicate y positions on the mean velocity profile by a subscript: y_a is the cross-stream location at which the mean velocity is equal to $U_{\min} + a(U_{\max} - U_{\min})$, where $U_{\min}$ and $U_{\max}$ are, respectively, the minimum and maximum values of $\langle U(y)\rangle$. For symmetric flows, the plane or axis of symmetry is at $y = 0$; for the plane mixing layer, the splitter plate is at $y = 0$ (Fig. 1). The flow widths are then defined as $\delta \equiv y_{0.5}$ for the three symmetric flows and as $\delta \equiv y_{0.1} - y_{0.95}$ for the plane mixing layer. These definitions are consistent with the bulk of the experimental literature.

Both analysis and experiment indicate that all of these flows become self-preserving sufficiently far downstream of the splitter plate, nozzle, or wake-generating body.[22–24] (Strictly speaking, self-similarity in a turbulent flow is possible only in the limit as the Reynolds number approaches infinity, so that viscosity has a negligible direct effect on the mean flow.[25] Nevertheless, it is customary in the turbulence literature to refer to flows where suitably normalized profiles of mean quantities become independent of the streamwise

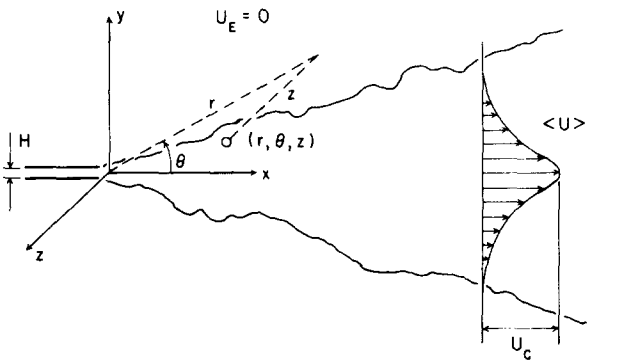

FIG. 3. The turbulent plane jet.

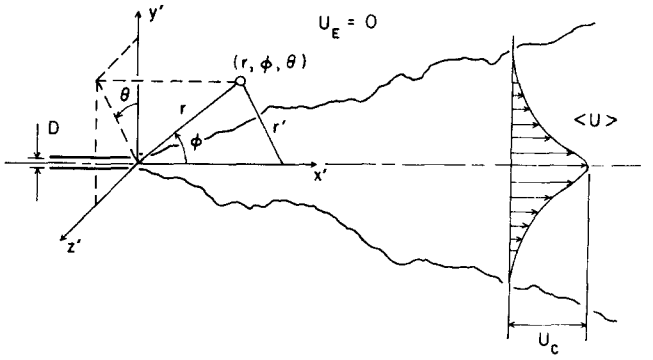

FIG. 4. The turbulent axisymmetric jet.

coordinate as self-similar or self-preserving, and the same convention is adopted here.) With zero streamwise mean pressure gradient in the free stream, exact self-similarity is achieved for the plane mixing layer for any value of the velocity ratio U_L/U_H $(0 \leqslant U_L/U_H \leqslant 1)$. Exact self-similarity is also attained for the plane and axisymmetric jets issuing into stagnant surroundings. The plane wake with zero free-stream mean pressure gradient is only asymptotically self-similar, i.e., the equations for the mean motion admit a self-similar solution in the limit as $x \to \infty$. For the exactly self-similar flows, the spreading rate $S = d\delta/dx$ is a constant. For the asymptotically self-similar plane wake, the flow width δ increases as $(x - x_0)^{1/2}$, while the peak velocity deficit U_D decays as $(x - x_0)^{-1/2}$, where x_0 is a virtual origin. It is customary in this case to take as a measure of the spreading rate $S = \frac{1}{2}\, d(U_E \delta U_D^{-1})/dx$, which is a constant. In the remainder of the paper, we will not distinguish between exact and asymptotic self-similarity.

In the self-similar regimes, profiles of any one-point statistic of the Eulerian velocity field (normalized by ΔU) can be rendered independent of x by introducing a similarity variable η. For the plane mixing layer, we take $\eta \equiv (y - y_{0.5})/\delta$, and for each of the three symmetric flows, $\eta \equiv y/\delta$. The velocity-composition joint pdf also becomes a function of the single spatial variable η and is independent of time in the self-similar flows. Velocity and length scales (ΔU and δ), spreading rates, and similarity variables for each of the four flows are summarized in Table I.

TABLE I. Definitions of scales, spreading rates, and similarity variables for four self-similar free shear flows.

Flow	Velocity scale ΔU	Width δ	Spreading rate S	Similarity variable η
Plane mixing layer	$U_H - U_L$	$y_{0.1} - y_{0.95}$	$\dfrac{d\delta}{dx}$	$\dfrac{y - y_{0.5}}{\delta}$
Plane wake	U_D	$y_{0.5}$	$\dfrac{1}{2}\dfrac{d}{dx}\left(\dfrac{U_E\delta}{U_D}\right)$	$\dfrac{y}{\delta}$
Plane jet	U_C	$y_{0.5}$	$\dfrac{d\delta}{dx}$	$\dfrac{y}{\delta}$
Axisymmetric jet	U_C	$y_{0.5}$	$\dfrac{d\delta}{dx}$	$\dfrac{y}{\delta}$

B. Experimental data

The experimental literature for the self-similar free shear flows is extensive. While for some flows, there appears to be a consensus on the most appropriate values for the spreading rates and on the "true" mean velocity profiles, there remains considerable disagreement in general among the results reported by different workers. Measured profiles of the normalized Reynolds shear stress $\langle uv \rangle/\Delta U^2$, which can be deduced from the mean velocity profile under the assumption of self-similarity, vary considerably from experiment to experiment.[23] The detailed distributions of turbulent kinetic energy

$$k \equiv \langle u_i u_i \rangle/2 = (\langle u^2 \rangle + \langle v^2 \rangle + \langle w^2 \rangle)/2$$

among the components $\langle u^2 \rangle$, $\langle v^2 \rangle$, and $\langle w^2 \rangle$ show even more variation. This may be seen clearly in the figures to be presented in Sec. V, where we compare our model calculations with experimental data.

The main reason for this scatter appears to be the difficulties inherent in hot-wire anemometry,[26] the measurement technique used in virtually all cases, coupled with effects of the experimental apparatus used, e.g., room draughts, wall effects, initial conditions, etc. Self-similarity is achieved only quite far downstream for some of these flows. Turbulence levels are then very low, making accurate measurements difficult and magnifying the effects of free-stream turbulence and room draughts. Specific measurement difficulties for each of the flows are discussed in what follows.

A critical review of experimental data in constant density self-similar free turbulent boundary layer flows is given by Rodi,[23] who concentrated on the more recent data available at that time (1975). Rodi assesses measurements of the spreading rate, streamwise mean velocity, Reynolds shear stress $\langle uv \rangle$, and turbulent kinetic energy k. He also discusses the balances in the shear stress and turbulent kinetic energy equations, but these are not of immediate interest to the present study. The reliability of the measurements was evaluated primarily on the basis of consistency checks: first, mean streamwise momentum should be conserved (symmetric flows only); and second, the measured Reynolds shear stress should agree with the value determined from the mean velocity profile and self-similarity. Rodi made recommendations as to which are the best data to take as target values for modelers.

We use Rodi's review as a guideline, supplementing it with more recent information when available. In all cases, we find it prudent to retain more than a single data set for comparison with our model. Consistency checks alone say nothing about the distribution of energy among the three diagonal components of the Reynolds stresses. It is the $\langle uv \rangle$ component of the Reynolds stresses that is of primary importance in these free shear flows, since that component affects the mean flow directly and is responsible for the production of turbulent kinetic energy. Nevertheless, it is important to see if the model gives the proper distribution of energy among the normal stresses; this is a test of the model-

ing of the fluctuating pressure gradient, which redistributes energy among the diagonal components of the Reynolds stress tensor.[22] Recent experimental studies suggest that there may be no unique self-preserving state for some of these flows; no detailed study of the effect of initial conditions is offered here.

1. Plane mixing layer ($U_L = 0$)

By contrast with the three symmetric flows, there is little agreement among the different experimenters' measured spreading rates for the plane mixing layer. This is attributed variously to the extreme streamwise distance required to achieve self-similarity of the mean velocity and Reynolds stress profiles ($\mathrm{Re}_x \equiv U_H x/\nu \approx 2 \cdot 10^5$, according to Champagne *et al.*[27]), to the effect of initial and boundary conditions in the experimental setup, to the relatively strong sensitivity of this flow to the external flow field (room draughts, free-stream turbulence, etc.), and to different hot-wire correction techniques.[23,27,28] Rodi recommends a spreading rate of 0.16 based on $y_{0.1} - y_{0.9}$; this corresponds to $d\delta/dx \approx 0.18 - 0.19$ for $\delta = y_{0.1} - y_{0.95}$ (Table I).

Based on the $\langle uv \rangle$ consistency check, Rodi recommends the data of Patel.[28,29] The more recent data of Champagne *et al.*[27] is quite similar to Patel's both in the spreading rate and in the distribution of energy among the normal stresses. Unfortunately, Champagne *et al.* did not present a $\langle uv \rangle$ profile. These two data sets are thus taken for comparison with our modeled results. Although Rodi found their $\langle uv \rangle / \Delta U^2$ peak to be too low, Wygnanski and Fiedler's[30] measurements are used as well. Their peak turbulent kinetic energy (normalized by ΔU^2) is about 25% greater than that of Champagne *et al.*, but it is of interest to retain their data set to illustrate the level of variation that exists between modern data sets. Wygnanski and Fiedler are also the only ones of these three to present measurements of the intermittency factor profile.

2. Plane wake behind a circular cylinder

While it may be expected that the self-similar far wake should be independent of the details of its generation (i.e., shape of wake generating body), it was observed by Rodi[23] that in fact, the initial conditions exert an influence far downstream. More recently, the lack of universality in small deficit plane turbulent wakes was investigated by Wygnanski *et al.*[31] We therefore confine our attention to the plane wake behind a single geometry of generator, the circular cylinder. A spreading rate of $S = 0.098$ is then supported by the bulk of the measurements up to 1975.[23]

Rodi recommends the generation-old data of Townsend[32] based on consistency of the $\langle uv \rangle$ profile, while cautioning that Townsend's turbulent kinetic energy levels may be somewhat low. Townsend's data also show the puzzling result that $\langle v^2 \rangle$ is greater than $\langle u^2 \rangle$ near the symmetry plane, contrary to observations in the other free shear flows. The more recent data of Fabris[33] show a mean velocity profile that is consistent with Townsend's, and a spreading parameter of $S = 0.096$. The distribution of energy among the components shows a more conventional behavior, with $\langle u^2 \rangle > \langle v^2 \rangle \approx \langle w^2 \rangle$ near the symmetry plane, but Fabris' peak shear stress $\langle uv \rangle / \Delta U^2$ appears to be too low. Intermittency factor profiles were presented both by Townsend and by Fabris. Here again, Townsend's measurements indicate that the plane wake differs from the other free shear flows in that the intermittency factor profile is much less steep for the plane wake than for the others. Like Fabris, Thomas[34] also suggests that the plane wake is not as dissimilar from the other free shear flows as Townsend's data indicate.

We take both Townsend's and Fabris' data for comparison with our model; the intermittency factor and normal stresses of Fabris are probably more reliable, while the $\langle uv \rangle$ profile of Townsend appears to be the better of the two. Townsend reports self-similarity of the mean velocity and Reynolds stress profiles for x/D greater than approximately 500, while Fabris reports $x/D = 400$ as sufficient. Thomas' measurements were taken at $x/D = 160$, and thus are not used here.

3. Plane jet

Measured mean velocity profiles obtained by different experimenters for the self-similar plane jet show significant disagreement near the outer edge, where the hot-wire technique used to obtain most of the profiles becomes suspect. One mean velocity measurement was made using an impact tube, that of Robins,[35] and this is the profile recommended by Rodi. The hot-wire profile of Heskestad[36] is quite close to Robins' data.

Rodi recommends a spreading rate of 0.11, the value measured by Heskestad; other workers report values that vary from 0.087 to 0.128.[37] This anomaly appears to be satisfactorily resolved by the analysis of Kotsovinos[37] and Bradshaw.[38] Kotsovinos observes that the larger the x/H at which the data are taken, the larger the reported spreading rate. He concludes that the data suggest a growth rate for the plane jet that is not exactly linear. Bradshaw then shows that this result is tentatively attributable to room draughts in the laboratory, and suggests that the most appropriate spreading rate in the absence of such draughts is at the lower end of the reported values, 0.091. We take the middle ground, and adopt $d\delta/dx = 0.10$ as the target spreading rate for our calculations. This is the same value recommended by Looney and Walsh[39] in their modeling study of plane jets.

For turbulence quantities, Rodi recommends Bradbury's data,[40] in spite of the fact that Bradbury used a low-speed coflowing stream, and thus could not achieve exact self-similarity. Rodi (and Bradbury) argue that departures from self-similarity are not significant in the range of x/H for which data are reported, and that the increased reliability in hot-wire measurements of the Reynolds stresses near the jet edge resulting from the nonzero mean velocity there more than compensates for the loss of exact self-similarity. Bradbury, however, reports $\langle v^2 \rangle$ to be greater than $\langle u^2 \rangle$ at the center of the jet, so although we accept his $\langle uv \rangle$ profile, the more recent data of Gutmark and Wygnanski[41] are considered as a more reasonable distribution of energy among the normal components; they report a spreading rate of 0.10 and their peak $\langle uv \rangle / \Delta U^2$ is consistent with Bradbury's. Heskestad's energy distribution is similar to that of Gutmark and Wygnanski, but his reported peak $\langle uv \rangle / \Delta U^2$ is lower than

indicated by his mean velocity profile, and his $\langle u^2\rangle/\Delta U^2$ profile shows a rather strong dependence on Re_H, the Reynolds number based on the jet slot width H. These difficulties are discussed further by Everitt and Robins.[42]

Two other papers that are of general interest in understanding the differences among various investigators' results for the plane jet are those of Kotsovinos[43] and Schneider.[44] These authors argue that contrary to the usual assumption that the momentum flux is conserved in thin jet flows,[22–24] it in fact decreases with x.

All three works (Heskestad,[36] Bradbury,[40] and Gutmark and Wygnanski[41]) present intermittency factor profiles. The differences are mainly at the outer edge, where the profile of Bradbury goes to zero more quickly than the other two. Gutmark and Wygnanski attribute this difference to the effect of room draughts, which were minimized in their facility by the use of screens around the jet. Heskestad's profile shows a rather slow approach to $\gamma = 1$ at the jet centerline; Gutmark and Wygnanski's profile appears to be the most appropriate one. They report that self-similarity of the mean velocity and Reynolds stress profiles was achieved at $x/H \approx 40$, and Heskestad, not until $x/H \approx 65$.

4. Axisymmetric jet

Compared to the flows discussed so far, there are relatively few recent data sets available for the self-similar axisymmetric jet. The two sets of data that we will use are those of Wygnanski and Fiedler[45] and Rodi.[46] Both report a spreading rate of 0.086, show similar mean velocity profiles, and show reasonable agreement in the measured normal stresses. The main difference is in the $\langle uv\rangle$ profile. Wygnanski and Fiedler's peak $\langle uv\rangle/\Delta U^2$ is lower than their $\langle U\rangle$ profile indicates (they report it as being consistent, but Rodi[23] finds it to be too low when the normal stress terms are retained in the axial momentum equation), while by using a different correction technique in the hot-wire measurements, Rodi achieves a consistent $\langle uv\rangle$ profile. Only Wygnanski and Fiedler show an intermittency factor profile, and this is in agreement with the much earlier measurements of Corrsin and Kistler.[47] Wygnanski and Fiedler find that the self-similar region begins at $x/D \approx 70$, while Rodi reports a slightly lower value, $x/D < 62$.

C. Summary

The nature of the self-similar free shear flows has been outlined, and the experimental literature has been reviewed to select data for the modeling study. Substantial deviations are found to exist among various experiments in nominally the same flow. At least two data sets are retained for each of the four flows. These data are shown in the figures presented in Sec. V, where the model's performance is evaluated based on a comparison with experimental results.

III. MODELING

The transport equation for the velocity-composition joint pdf is modeled by adopting a Lagrangian approach, where we consider the behavior of fluid particles in a turbulent flow. Five models are described for the particle velocities; the generalized Langevin equation is discussed in most detail. It is found that the set of model constants presented in Ref. 1 for homogeneous flows gives poor performance in the free shear flows; modified values are recommended that give better agreement in the shear flows with minimal degradation of results in the flows studied earlier. Models for molecular diffusivity, the turbulent time scale or dissipation rate, and intermittency are presented briefly.

A. The pdf evolution equation

We define $f(\mathbf{V},\Psi;\mathbf{x},t)$ to be the joint probability density of the event $\{\mathbf{U}(\mathbf{x},t) = \mathbf{V}, \Phi(\mathbf{x},t) = \Psi\}$. If $Q(\mathbf{U},\Phi)$ is any function of the Eulerian velocity and scalar fields, the mean value of Q at any position $\mathbf{x}$ and time t can be expressed as an integral over the pdf,

$$\langle Q(\mathbf{x},t)\rangle = \int\int Q(\mathbf{V},\Psi) f(\mathbf{V},\Psi;\mathbf{x},t)\, d\mathbf{V}\, d\Psi, \tag{1}$$

where $\int d\mathbf{V}$ represents integration over the entire three-dimensional velocity space and $\int d\Psi$ represents integration over the composition space. This one-point joint pdf contains all one-point statistical information about the Eulerian velocity and scalar fields. A transport equation for $f(\mathbf{V},\Psi;\mathbf{x},t)$ can be derived from the Eulerian conservation equations for $\mathbf{U}(\mathbf{x},t)$ and $\Phi(\mathbf{x},t)$.[2,10] In a constant-density flow, the terms to be modeled in the pdf equation are those representing the effects of viscous dissipation, the fluctuating pressure gradient, and molecular diffusion.

Rather than modeling the unclosed terms in the pdf equation directly, it is convenient to adopt a Lagrangian viewpoint. Modeling the behavior of fluid particles in a turbulent flow effectively provides closure models for the unclosed terms in the pdf evolution equation.[2] At time t, the position, velocity, and composition (a conserved passive scalar) of a fluid particle are denoted by $\mathbf{x}^+(t)$, $\mathbf{U}^+(t)$, and $\Phi^+(t)$. By definition, the rate of change of position of a fluid particle is its velocity; the velocity changes in accordance with the Navier–Stokes equation; and, the scalar evolves by the conservation equation for a conserved passive scalar. In an increment of time dt, then, the increments in fluid particle position, velocity, and composition are given by[2]

$$dx_i^+ = U_i^+\, dt, \tag{2}$$

$$dU_i^+ = -\frac{1}{\rho}\frac{\partial\langle p\rangle}{\partial x_i}\, dt + \left(\nu\nabla^2 u_i - \frac{1}{\rho}\frac{\partial p'}{\partial x_i}\right) dt, \tag{3}$$

$$d\Phi^+ = \Gamma\nabla^2\Phi'\, dt. \tag{4}$$

In these equations, the Eulerian velocity, pressure, and scalar fields have been decomposed into their means $\langle\mathbf{U}(\mathbf{x},t)\rangle$, $\langle p(\mathbf{x},t)\rangle$, and $\langle\Phi(\mathbf{x},t)\rangle$ and fluctuations $\mathbf{u}(\mathbf{x},t)$, $p'(\mathbf{x},t)$, and $\Phi'(\mathbf{x},t)$. These Eulerian quantities are evaluated at the particle position $\mathbf{x}^+(t)$. The fluid properties are the (constant) density ρ, the kinematic viscosity ν, and the molecular diffusivity Γ. Two terms, $\nu\nabla^2\langle U\rangle$ and $\Gamma\nabla^2\langle\Phi\rangle$, have been neglected, as is appropriate in a high Reynolds number (high Peclet number) turbulent flow. Since the mean Eulerian fields can be expressed in terms of the one-point pdf using Eq. (1) (for the mean pressure, via a Poisson equation[2]), it is necessary only to model the fluctuating terms on the right-

hand sides of Eqs. (3) and (4). Convective transport in physical space is treated exactly [Eq. (2)].

B. Viscosity and fluctuating pressure gradient

The terms to be modeled in Eq. (3) are the viscous and fluctuating pressure gradient terms. Five models are presented for these effects. The first is the generalized Langevin equation of Ref. 1; this is intended to be applicable to turbulent flows subjected to arbitrary mean strains. The remaining four are computationally simpler models that are expected to be of more limited applicability. Three of these are simplified versions of the Langevin equation, and the final one is the particle interaction model described in Ref. 2. These simpler models are studied with the intention of finding a computationally simple yet robust model for use in turbulent shear flows.

The differences among these models may best be understood by comparing the resulting modeled Reynolds stress equations. This equation is given for the four simpler models; the modeled Reynolds stress equation corresponding to the generalized Langevin model is quite lengthy and is given in Ref. 1.

1. Generalized Langevin equation (GL)

According to the generalized Langevin model,[1] the increment in particle velocity $\mathbf{U}^*(t)$ in a time interval dt is given by

$$dU_i^* = -\frac{1}{\rho}\frac{\partial \langle p \rangle}{\partial x_i}\,dt + G_{ij}(U_j^* - \langle U_j \rangle)dt + (C_0\epsilon)^{1/2}\,dW_i(t), \tag{5}$$

that is, the particle velocity is governed by a stochastic differential equation of the Langevin type. The notation * is used to distinguish this modeled particle from a fluid particle. In Eq. (5), $G_{ij}(\mathbf{x},t)$ is a function of one-point statistics of the velocity field (i.e., it is a function of the one-point pdf), $\epsilon(\mathbf{x},t)$ is the dissipation rate of turbulent kinetic energy, C_0 is a universal constant, and $\mathbf{W}(t)$ is an isotropic Wiener process. This is a Markovian stochastic process whose increments $d\mathbf{W}(t) = \mathbf{W}(t+dt) - \mathbf{W}(t)$ have a joint-normal distribution with zero means and an isotropic covariance matrix,

$$\langle dW_i(t) \rangle = 0, \quad \langle dW_i(t)\,dW_j(t) \rangle = dt\,\delta_{ij}. \tag{6}$$

It is shown in Ref. 1 that Eq. (5) provides a closure model for the viscous and fluctuating pressure gradient terms in the pdf evolution equation, provided that $\epsilon(\mathbf{x},t)$ is known. The dissipation model is discussed below. It is the sum of the two modeled terms in Eq. (5) that jointly represent the effects of viscosity and the fluctuating pressure. It can be shown[1] that the random term in Eq. (5) leads to an increase in the turbulent kinetic energy k, while viscous dissipation causes k to decay, and the fluctuating pressure redistributes energy among the components of the Reynolds stress leaving k unchanged (in constant-density flow). Thus the decrement in turbulent kinetic energy corresponding to the term containing G_{ij} in Eq. (5) must account for the viscous dissipation as well as compensating for the energy added by the isotropic Wiener process. This leads to a constraint relating G_{ij} and C_0.[1]

This Langevin model can be viewed as an analogy between the velocity of a fluid particle in a turbulent flow and the velocity of a particle undergoing Brownian motion. It yields a joint-normal distribution for the velocity joint pdf $f_U(\mathbf{V};\mathbf{x},t)$ in homogeneous flows, in agreement with experimental data, it is consistent with Kolmogorov's inertial-range scaling hypotheses of 1941, and it satisfies realizability.[1,2] The value of the universal (Kolmogorov) constant C_0 is taken to be 2.1, following Anand and Pope.[14]

Haworth and Pope[1] proposed a functional form for G_{ij} that is linear in the mean velocity gradients $\partial \langle U_p \rangle / \partial x_q$ and in the Reynolds stresses $\langle u_k u_l \rangle$:

$$G_{ij} = \frac{\alpha_1 \delta_{ij}}{\tau} + \frac{\alpha_2 b_{ij}}{\tau} + H_{ijkl}\frac{\partial \langle U_k \rangle}{\partial x_l}, \tag{7}$$

where

$$H_{ijkl} = \beta_1\delta_{ij}\delta_{kl} + \beta_2\delta_{ik}\delta_{jl} + \beta_3\delta_{il}\delta_{jk} + \gamma_1\delta_{ij}b_{kl} + \gamma_2\delta_{ik}b_{jl} + \gamma_3\delta_{il}b_{jk} + \gamma_4 b_{ij}\delta_{kl} + \gamma_5 b_{ik}\delta_{jl} + \gamma_6 b_{il}\delta_{jk}. \tag{8}$$

Here b_{kl} is the normalized anisotropy tensor defined by

$$b_{kl} = \langle u_k u_l \rangle / 2k - \tfrac{1}{3}\delta_{kl}, \tag{9}$$

and τ is the dissipation time scale,

$$\tau \equiv k/\epsilon. \tag{10}$$

The model contains 11 coefficients. Of these 11, seven degrees of freedom are eliminated by exact constraints deduced from the Navier–Stokes equation. The remaining four coefficients, assumed to be constants, are determined empirically by matching the modeled evolution of the Reynolds stresses to experimental data in homogeneous turbulent flows. A set of constants was presented such that the modeled evolution of the Reynolds stresses matches experimental data in virtually every homogeneous flow for which data are available. When this same model (with the same values for the model constants) is applied to the plane mixing layer,[15] it is found that the calculated spreading rate is a factor of 3 to 4 lower than experimental values, and calculated turbulence intensities are correspondingly low. The same has been found to be true for the other free shear flows. We now know that this is, in part, a result of the boundary-layer solution algorithm used in these earlier calculations (see Sec. IV). This is not sufficient to explain such large discrepancies, however. Some changes in the model constants from the optimum values reported in Ref. 1 are necessary to give reasonable results for the free shear flows.

A sensitivity analysis in the homogeneous flows[1] revealed that a single linear combination of the four model constants dominates the modeled evolution of the Reynolds stresses. Not surprisingly, we find that it is the same group to which the calculated spreading rates of the free shear flows are most sensitive. Unfortunately, then, we cannot change the model constants in a way that gives good results for the free shear flows without degrading the results for the homogeneous shear flows. It appears that the only way to achieve good results in both sets of flows is to relax one of the constraints on the model coefficients.

In Ref. 1, a constraint proposed by Speziale[48] was ap-

TABLE II. Summary of model constants.

Model	Constant	Value
Generalized Langevin model (GL)	α_2	3.78
	β_1	−0.20
	β_2	0.80
	β_3	−0.20
	γ_1	−1.24
	γ_2	1.04
	γ_3	−0.34
	γ_4	0.00
	γ_5	1.99
	γ_6	−0.76
First intermediate Langevin model (IL1)	α_2	$3.7 - 4.0\,P/\epsilon$
Second intermediate Langevin model (IL2)	β_2	0.25
	β_3	0.05
Particle interaction model (PI)	C_1	4.5
Scalar mixing model	C_ϕ	2.00
Intermittency model	C_g	2.0
	C_m	1.5
	C_e	5.0

plied so that the modeled Reynolds stress evolution equation transforms properly in the limit of two-dimensional turbulence (where one eigenvalue of the Reynolds stress tensor is zero). It was pointed out that such a limit is, in a strict sense, beyond the scope of this model. Moreover, both the homogeneous flows studied there and the free shear flows considered here are quite far from this limit. By relaxing this constraint, we are able to get reasonable results for the free shear flows. In fact, since the Speziale constraint need only be satisfied in the limit of two-dimensional turbulence, we can still satisfy it exactly by making one or more of our coefficients a function of the eigenvalues of the Reynolds stress tensor in such a way that the constraint is satisfied whenever one eigenvalue is zero. No attempt is made to construct such a functional form here. Assuming that all coefficients are constants, we find that we get reasonable agreement for the spreading rates of the free shear flows using the values of the constants shown in Table II (the notation used is that of Ref. 1).

The set of constants given in Table II gives results in the homogeneous flows that are virtually indistinguishable from those reported in Ref. 1, with one exception: the normalized shear stress $\langle uv\rangle/2k$ for the strongly sheared homogeneous shear flows (Harris *et al.*[49] and Tavoularis and Corrsin[50]) is overpredicted by about 25%. The distribution of energy among the normal components of the Reynolds stress tensor remains good in these flows, however.

2. Simplified Langevin equation (SL)

The simplified Langevin model is a special case of Eq. (5), where G_{ij} is isotropic and is independent of $\langle u_k u_l\rangle$ and of $\partial\langle U_p\rangle/\partial x_q$. It can be shown[1,2,14] that in order for the turbulent kinetic energy k to evolve properly, G_{ij} is related to C_0 by

$$G_{ij} = -(\tfrac{1}{2} + \tfrac{3}{4}C_0)\delta_{ij}/\tau. \tag{11}$$

The evolution of the Reynolds stresses according to this model is[1]

$$\frac{\partial\langle u_k u_l\rangle}{\partial t} + \langle U_i\rangle\frac{\partial\langle u_k u_l\rangle}{\partial x_i} + \frac{\partial\langle u_k u_l u_i\rangle}{\partial x_i} + \langle u_k u_i\rangle\frac{\partial\langle U_l\rangle}{\partial x_i} + \langle u_l u_i\rangle\frac{\partial\langle U_k\rangle}{\partial x_i} = -(3C_0+2)\epsilon b_{kl} - \tfrac{2}{3}\epsilon\delta_{kl}, \tag{12}$$

where b_{kl} is the normalized anisotropy tensor of Eq. (9). It may be seen that Eq. (12) corresponds to Rotta's linear return-to-isotropy model for the Reynolds stresses[20,51] with the Rotta constant C_1 given by (with $C_0 = 2.1$)

$$C_1 = (3C_0 + 2)/2 = 4.15. \tag{13}$$

This is somewhat higher than the value $C_1 = 1.5$ recommended by Launder *et al.*,[20] but is is close to the value $C_1 = 4.5$, which is found to yield good results in free shear flows in the absence of an explicit model for the "rapid" pressure terms,[52] that is, terms involving the mean velocity gradients.

3. First intermediate Langevin model (IL1)

Two other models based on a Langevin equation are evaluated. These are intermediate in complexity between the generalized Langevin model of Sec. III B 1 and the simplified model of Sec. III B 2.

The first intermediate Langevin model retains those terms in G_{ij} that involve the normalized anisotropy tensor b_{kl} [the α_1 and α_2 terms in Eq. (7)]. Applying the turbulent kinetic energy constraint [Eq. (25) of Ref. 1], which gives α_1 in terms of α_2, we find that the Reynolds stresses evolve by

$$\frac{\partial\langle u_k u_l\rangle}{\partial t} + \langle U_i\rangle\frac{\partial\langle u_k u_l\rangle}{\partial x_i} + \frac{\partial\langle u_k u_l u_i\rangle}{\partial x_i} + \langle u_k u_i\rangle\frac{\partial\langle U_l\rangle}{\partial x_i} + \langle u_l u_i\rangle\frac{\partial\langle U_k\rangle}{\partial x_i} = -(3C_0 + 2 - \tfrac{4}{3}\alpha_2)\epsilon b_{kl} + 4\alpha_2\epsilon\left[b_{ki}b_{il} - b_{ii}^2(b_{kl} + \tfrac{1}{3}\delta_{kl})\right] - \tfrac{2}{3}\epsilon\delta_{kl}. \tag{14}$$

This corresponds to Rotta's model with the Rotta constant

$$C_1 = (3C_0 + 2 - \tfrac{4}{3}\alpha_2)/2 = 4.15 - \tfrac{2}{3}\alpha_2, \tag{15}$$

plus higher-order terms in the normalized anisotropy tensor.

The value of α_2 is chosen by reference to experimental data in homogeneous shear flows. It is found the no single constant value yields good results both in the weakly sheared flow of Champagne *et al.*[53] and in the strongly sheared flows of Harris *et al.*[49] and Tavoularis and Corrsin.[50] Acceptable results are obtained by making α_2 be a function of the ratio of production P to dissipation ϵ of turbulent kinetic energy:

$$\alpha_2 = 3.7 - 4.0P/\epsilon, \tag{16}$$

where

$$P \equiv -\langle u_i u_j \rangle \frac{\partial \langle U_i \rangle}{\partial x_j}. \tag{17}$$

In decaying turbulence ($P/\epsilon = 0$), this gives $\alpha_2 = 3.7$, consistent with the value reported in Ref. 1.

4. Second intermediate Langevin model (IL2)

The second intermediate Langevin model retains the terms linear in the mean velocity gradient in G_{ij}, but no terms in the normalized anisotropy tensor. These are the α_1 and $\beta_1 - \beta_3$ terms in Eqs. (7) and (8). The value of β_1 is arbitrary in constant density flow; we choose $\beta_1 = 0$. This leaves two degrees of freedom in the model, since α_1 is again fixed by the turbulent kinetic energy constraint.[1] No additional constraints are applied (i.e., the rapid distortion constraints of Ref. 1), and the Reynolds stresses evolve by

$$\begin{aligned}
&\frac{\partial \langle u_k u_l \rangle}{\partial t} + \langle U_i \rangle \frac{\partial \langle u_k u_l \rangle}{\partial x_i} + \frac{\partial \langle u_k u_l u_i \rangle}{\partial x_i} \\
&\quad + \langle u_k u_i \rangle \frac{\partial \langle U_l \rangle}{\partial x_i} + \langle u_l u_i \rangle \frac{\partial \langle U_k \rangle}{\partial x_i} \\
&\quad = -[3C_0 + 2 - 2(\beta_2 + \beta_3)P/\epsilon]\epsilon b_{kl} \\
&\qquad - \beta_2 (P_{kl} - \tfrac{2}{3} P \delta_{kl}) - \beta_3 (D_{kl} - \tfrac{2}{3} P \delta_{kl}) - \tfrac{2}{3} \epsilon \delta_{kl},
\end{aligned} \tag{18}$$

where

$$P_{kl} = -\left(\langle u_k u_i \rangle \frac{\partial \langle U_l \rangle}{\partial x_i} + \langle u_l u_i \rangle \frac{\partial \langle U_k \rangle}{\partial x_i} \right), \tag{19}$$

$$D_{kl} = -\left(\langle u_k u_i \rangle \frac{\partial \langle U_i \rangle}{\partial x_l} + \langle u_l u_i \rangle \frac{\partial \langle U_i \rangle}{\partial x_k} \right), \tag{20}$$

$$P = -\langle u_i u_j \rangle \frac{\partial \langle U_i \rangle}{\partial x_j} = \frac{1}{2} P_{ii} = \frac{1}{2} D_{ii}. \tag{21}$$

This again has the form of Rotta's model for the return-to-isotropy of the Reynolds stresses with

$$C_1 = [3C_0 + 2 - 2(\beta_2 + \beta_3)P/\epsilon]/2, \tag{22}$$

together with a rapid pressure model that is intermediate in complexity between the two models presented by Launder *et al.*[20] The values $\beta_2 = 0.25$ and $\beta_3 = 0.05$ are chosen to yield good results in both the weakly sheared (Champagne *et al.*[53]) and strongly sheared (Harris *et al.*,[49] Tavoularis and Corrsin[50]) homogeneous shear flows.

5. Particle interaction model (PI)

The final model for the particle velocities is the particle interaction model. This consists of two parts: the improved stochastic mixing model[2,3] models the action of molecular diffusivity; and the stochastic reorientation model[2,10] models the fluctuating pressure gradient. The latter part again corresponds to Rotta's model, and the modeled Reynolds stress equation is

$$\begin{aligned}
&\frac{\partial \langle u_k u_l \rangle}{\partial t} + \langle U_i \rangle \frac{\partial \langle u_k u_l \rangle}{\partial x_i} + \frac{\partial \langle u_k u_l u_i \rangle}{\partial x_i} \\
&\quad + \langle u_k u_i \rangle \frac{\partial \langle U_l \rangle}{\partial x_i} + \langle u_l u_i \rangle \frac{\partial \langle U_k \rangle}{\partial x_i} \\
&\quad = -2C_1 \epsilon b_{kl} - \tfrac{2}{3} \epsilon \delta_{kl},
\end{aligned} \tag{23}$$

where C_1 is the Rotta constant. Note that in homogeneous flows, this is identical to the simplified Langevin Reynolds stress equation, Eq. (12), with C_1 given by Eq. (13). Here we choose $C_1 = 4.5$.

Unlike the models based on a Langevin equation, where each particle evolves independently, the particle interaction models are expressed as interactions between pairs of particles. Further details can be found in Ref. 2.

6. Summary

Five models for the velocity of a particle in a turbulent flow have been presented. Of these, only the generalized Langevin model is intended to be applicable to general flows. The others are studied to find a computationally simple and robust model that will work well in shear flows.

The modeled evolution of the normalized anisotropy tensor b_{kl} in the weakly sheared flow of Champagne *et al.*[53] ($P/\epsilon \approx 1.0$) and in the strongly sheared flow of Tavoularis and Corrsin[50] ($P/\epsilon \approx 1.7$) for each of the five models is shown in Figs. 5 and 6. Here the "1" direction is the streamwise direction, and the streamwise mean velocity increases linearly in the "2" direction. The dissipation time scale τ of Eq. (10) is extracted directly from the experimental data. Only the modeled evolution of b_{11}, b_{33}, and b_{12} is shown, for

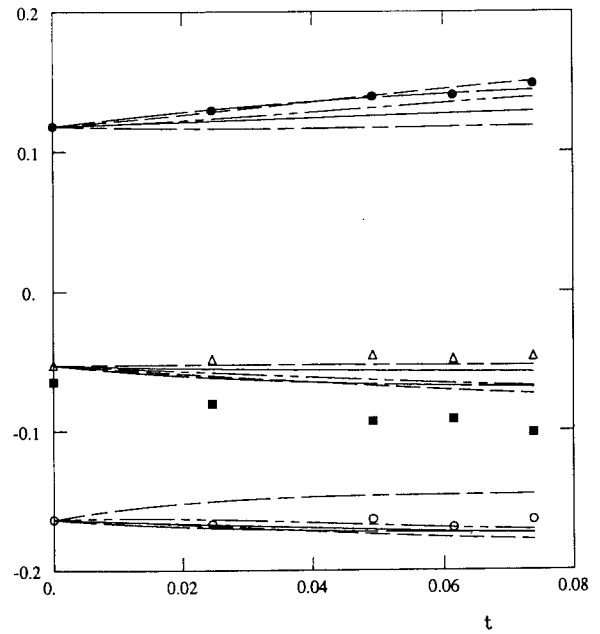

FIG. 5. Evolution of the normalized anisotropy tensor b_{kl} for the homogeneous shear flow experiment of Champagne *et al.*[53] Lines are computations, symbols are experimental data: —— GL; - - - - SL; — — IL1; — · — IL2; — -- — PI; ● b_{11}; ■ b_{22}; △ b_{33}; ○ b_{12}. Calculations are shown only for b_{11}, b_{33}, and b_{12}.

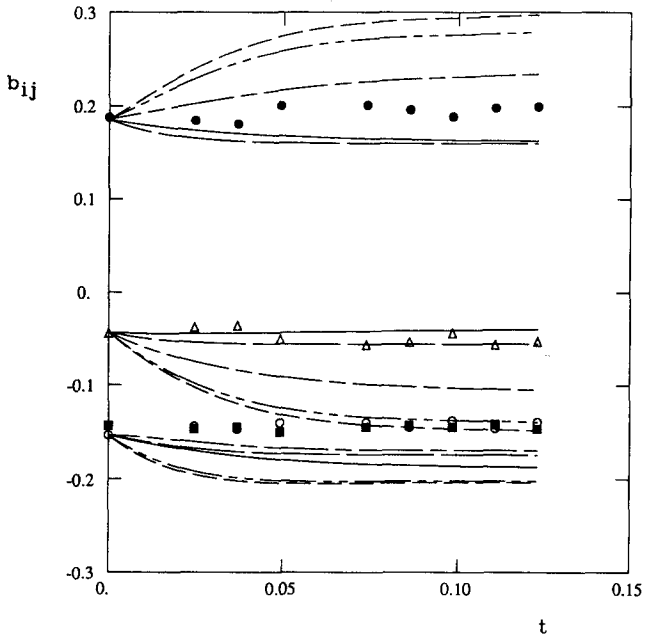

FIG. 6. Evolution of the normalized anisotropy tensor b_{kl} for the homogeneous shear flow experiment of Tavoularis and Corrsin.[50] Lines are computations, symbols are experimental data: —— GL; - - - - SL; — — IL1; — · — IL2; — · · — PI; ● b_{11}; ■ b_{22}; △ b_{33}; ○ b_{12}. Calculations are shown only for b_{11}, b_{33}, and b_{12}.

clarity; the component b_{22} can be deduced from the relationship $b_{11} + b_{22} + b_{33} = 0$.

All models do fairly well in the weakly sheared flow of Fig. 5 while substantial differences are evident in the strongly sheared flow of Fig. 6. Here the shear component b_{12} is somewhat overpredicted by all five models, with the simplified Langevin and particle interaction models showing the greatest error. The distribution of energy among the normal stresses is best for the generalized Langevin and first intermediate Langevin models and worst for the simplified Langevin and particle interaction models. The latter two models tend to put too much energy into the streamwise component $\langle u^2 \rangle$ in the strongly sheared flow.

C. Scalar mixing model

For the molecular diffusion term in Eq. (4), we adopt the scalar mixing model described in Ref. 3. This is essentially a modification of Curl's model[54] that gives the proper relaxation of the scalar pdf $f_\Phi(\Psi;\mathbf{x},t)$ to nearly a Gaussian distribution in homogeneous turbulence.[2,3] This model involves a single constant C_Φ which is the ratio of the turbulence time scale τ of Eq. (10) to the scalar time scale τ_Φ,

$$\tau_\Phi \equiv \langle \Phi'^2 \rangle / 2\epsilon_\Phi, \tag{24}$$

where ϵ_Φ is the molecular dissipation rate of the scalar variance $\langle \Phi'^2 \rangle$. We take $C_\Phi = 2.0$, the conventional value.[12]

D. Dissipation model

For these thin free shear flows, it is reasonable to argue that the turbulent time scale τ of Eq. (10) is constant across the flow.[12,15] Most experimental data are reasonably consistent with this assumption, at least in the fully turbulent core of the flow. Since the flows are self-similar, the turbulence time scale must be proportional to the mean flow time scale. In terms of the characteristic velocity ΔU and characteristic length δ for each flow (Table I), we can write

$$\omega \equiv 1/\tau = \omega^*(\Delta U/\delta), \tag{25}$$

where we take ω^* to be a constant. A value of ω^* for each flow is chosen first by attempting to deduce a reasonable value from the experimental data. Because of the extreme difficulty in measuring the dissipation rate ϵ directly, the accuracy of these values is suspect. We then fine tune ω^* to give approximately the correct peak value of $\langle uv \rangle / \Delta U^2$ for each flow. The value of ω^* is, in general, different for each of the five velocity models. Values of ω^* for each flow and for each model are given in Table III.

TABLE III. Choice of ω^* for each flow, for each model.

	GL	SL	IL1	IL2	PI
Plane mixing layer	0.200	0.210	0.175	0.165	0.200
Plane wake	0.135	0.170	0.160	0.138	0.145
Plane jet	0.154	0.195	0.204	0.143	0.158
Axisymmetric jet	0.176	0.208	0.234	0.146	0.170

Because there is a unique relationship between $\langle uv \rangle$ and $\langle U \rangle$ in the self-similar regime, and because the spreading rate S is defined by the $\langle U \rangle$ profile (Table I), it is expected that fixing the proper peak $\langle uv \rangle / \Delta U^2$ for each flow effectively fixes the proper mean velocity profile and spreading rate. The calculations are not entirely predictive in that we do not have a self-contained scale equation (a modeled transport equation for τ or for ϵ). This is consistent with our philosophy of concentrating on the particle velocity models in this study. Future work on dissipation modeling in the pdf method is discussed in Sec. VI.

E. Conditional modeling

Many experimental studies of free shear flows have shown that intermittency is important to the understanding of the physics of these flows.[27,30,32–34,41,45] Intermittency refers to a feature of turbulent free shear flows first noticed by Corrsin[55]: as the interface between turbulent and nonturbulent fluid moves, a fixed point in laboratory coordinates experiences a duty cycle such that for a fraction of time γ, it is in turbulent fluid and for a fraction of time $1 - \gamma$, it is in the irrotational free stream. Here $\gamma(\mathbf{x},t)$ is the intermittency factor. It is reasonable to expect that a model that takes explicit account of this phenomenon better captures the physics of the flow than one that does not, and should therefore give results in better agreement with experimental data. Other advantages of using conditional modeling are that it allows the modeler to calculate several quantities of interest that experimenters have been measuring for many years, such as profiles of the intermittency factor, statistics conditional on the fluid being turbulent, and statistics conditional on the fluid being nonturbulent; and, it helps with the specification of physically realistic boundary conditions (Sec. IV C). While the focus of the present investigation is a comparison of the more conventional unconditional averages with ex-

perimental data, we feel that it is appropriate to have some model, even one that is somewhat less than ideal, in place to account for intermittency.

To incorporate this effect, we adopt the conserved passive scalar approach introduced by Kollmann and Janicka.[4] The scalar $\Phi(\mathbf{x},t)$ takes on a value of unity in the outer irrotational flow of the wake and jets and in the high-speed stream of the plane mixing layer; it has the value zero in the low-speed stream of the mixing layer. The condition $\{0<\Phi(\mathbf{x},t)<1\}$ is then used to distinguish turbulent fluid from nonturbulent fluid. The intermittency factor $\gamma(\mathbf{x},t)$ is more rigorously defined as the probability of the fluid at position $\mathbf{x}$ and time t being turbulent. In terms of $\Phi(\mathbf{x},t)$, the intermittency factor is

$$\gamma(\mathbf{x},t) = \text{Prob}\{0<\Phi(\mathbf{x},t)<1\}. \tag{26}$$

In the Lagrangian viewpoint, a particle is turbulent if the value of its scalar $\Phi^*(t)$ lies between 0 and 1, $0<\Phi^*(t)<1$. The velocities of particles that are turbulent evolve according to the particle velocity model chosen (see Sec. III B), while nonturbulent particle velocities are affected only by the mean pressure gradient. This effectively neglects viscous dissipation and the fluctuating pressure gradient in the nonturbulent fluid [Eq. (3)]. Scales of motion in the nonturbulent fluid are not small enough for viscous dissipation to be significant, so the first assumption is justified. Similarly, the modeled molecular diffusivity term in Eq. (4) is neglected in the irrotational fluid. However, there are significant pressure fluctuations in the nonturbulent fluid. In Ref. 12, an examination of the experimental data revealed that the energy in the nonturbulent velocity fluctuations is generally quite small compared to the energy in the turbulent velocity fluctuations for these thin shear flows. Thus the velocity fluctuations caused by pressure fluctuations in the nonturbulent fluid appear to have little overall effect on the flow, justifying our neglect of the irrotational pressure fluctuations.

In the model, initially nonturbulent fluid [$\Phi^*(t)=0$ or $\Phi^*(t)=1$] is entrained [i.e., becomes turbulent, $0<\Phi^*(t)<1$] at a rate that is proportional to the local rate of production of turbulent kinetic energy.[12] The entrainment rate is controlled by a model constant C_g. Two additional model constants C_m and C_e control, respectively, the rate of momentum transfer between turbulent and nonturbulent fluid and the rate of energy transfer from the turbulent fluid. These models and their relationship to a conditionally modeled pdf equation are discussed in more detail in Ref. 12. There, values for these three constants were selected based on a modeling study of the self-similar turbulent plane jet using the particle interaction model of Sec. III B 5. In the current study, using different models for the particle velocity and looking at more than one kind of flow, we find that a higher value for C_g than was recommended in Ref. 12 seems appropriate: $C_g=2.0$ here versus 1.5 there. The values of C_m and C_e used in Ref. 12 are retained (see Table II).

F. Summary

Models have been described for four physical processes occurring in constant-density turbulent free shear flows: viscous dissipation, the fluctuating pressure gradient, molecular diffusion, and intermittency. All models have been expressed in Lagrangian form, that is, as models for fluid particle behavior. Scale information for this one-point closure is provided by specifying a constant normalized turbulent frequency ω^* across the flow [Eq. (25)]. With the exception of ω^*, the same values for the model constants are used in all of the calculations reported in Sec. V; these values are summarized in Table II. For GL, IL1, and IL2, α_1 is determined from Eq. (31) of Ref. 1, and the value of all other constants not given in Table II is zero for these three models. Values of ω^* for each flow and each model are given in Table III.

IV. SOLUTION ALGORITHMS

The modeled joint pdf transport equation is solved by a Monte Carlo method. In this approach, we track the trajectories of a large number N of particles in the velocity-composition-position state space using the models described in Sec. III. Two different algorithms are employed, one for the plane mixing layer, plane jet, and axisymmetric jet and a different one for the plane wake. In both cases, the problem is amenable to an essentially one-dimensional (in physical space) treatment. Details of the numerical methods are given elsewhere[2,5]; here we outline only the basic features of the algorithms and the boundary conditions imposed for each flow.

A. Boundary-layer algorithm

These thin free shear flows are characterized by a single predominant flow direction x (Figs. 1–4). A solution algorithm appropriate to this case is described in Sec. 6.8 of Ref. 2. Particles are marched downstream in fixed steps Δx, in essence replacing the x coordinate by time. The flows are statistically homogeneous in the z direction; thus only the single position coordinate y need be retained for each particle. This method is limited to flows where there is a negligible probability of particles having a negative streamwise velocity, a condition that is satisfied for small deficit wake flows ($U_E \gg U_D$, Fig. 2) or for a high velocity ratio plane mixing layer (U_L/U_H close to unity, Fig. 1). But this condition is violated for low velocity ratio plane mixing layers ($U_L/U_H \to 0$) or for jets issuing into stagnant surroundings. In particular, spreading rates and velocity ratios calculated using this technique are too low for the latter group of flows.[5] An earlier modeling study of the zero velocity ratio plane mixing layer[15] used this method; it is now realized that the numerical errors resulting from the inappropriate application of this algorithm are partially responsible for the low calculated spreading rate and turbulence intensities reported there. In the current study, the boundary-layer algorithm is used only for the plane wake.

B. Self-similar algorithm

For the remaining three flows, an alternative algorithm is used that takes direct advantage of the self-preserving nature of the flows and that is not subject to the limitations noted above for the boundary-layer algorithm at velocity

ratios near zero. The plane mixing layer is self-similar in the cylindrical coordinate system of Fig. 1 with the statistics of U_r, U_θ, and U_Z being independent of r. Thus the joint pdf $f_U(V_r,V_\theta,V_Z;r,\theta,z,t)$ is independent of r (self-similarity) and independent of z (statistical homogeneity). The self-similar plane jet is also conveniently described in cylindrical coordinates (Fig. 3); here it is the statistics of $r^{1/2}U_r$, $r^{1/2}U_\theta$, and $r^{1/2}U_Z$ that become independent of r in the self-similar regime. Thus $f_U(r^{1/2}V_r,r^{1/2}V_\theta,r^{1/2}V_Z;r,\theta,z,t)$ becomes independent of r and independent of z. For the axisymmetric jet, the spherical coordinate system shown in Fig. 4 is most appropriate; the statistics of rU_r, rU_ϕ, and rU_θ become independent of r, so the pdf $f_U(rV_r,rV_\phi,rV_\theta;r,\phi,\theta,t)$ is a function of ϕ only in physical space (the flow is statistically homogeneous in θ). In each case, the dimensionality of the pdf in physical space is reduced to one. These self-preserving flows are also statistically stationary, but we retain the time dependence of the pdf: the solution algorithm consists of marching in time from (almost) arbitrary initial conditions until the stationary, self-similar solution is attained. For further details, see Ref. 5.

In both of these algorithms, only a single position coordinate need be retained for each particle. We solve at a fixed value of r, $r=1$, for convenience. Denoting the retained coordinate by y, the solution domain is divided into K cells of width Δy, the k th centered at y_k. An estimate of the mean of any function of the velocities and scalars $Q(\mathbf{U},\Phi)$ at y_k is the ensemble average over the N_k particles in cell k,

$$\langle Q(y_k)\rangle \approx \langle Q(y_k)\rangle_{N_k} = \frac{1}{N_k}\sum Q(\mathbf{U}^{(n)},\Phi^{(n)}). \quad (27)$$

Statistics conditional on the fluid being turbulent or nonturbulent are estimated similarly by averaging over only the turbulent, or only the nonturbulent particles within each cell; the intermittency factor at y_k is given approximately by the fraction of turbulent particles in cell k.

While this ensemble averaging is conceptually useful, it is of limited practicability. The statistical error is of order $N_k^{-1/2}$, where $N_k \approx N/K$, and derivatives of mean quantities estimated in this manner are hopelessly inaccurate for reasonable values of N[2]. A more satisfactory technique for extracting profiles of mean quantities is the method of cross-validated least squares cubic splines, a curve fitting method that minimizes the statistical error.[2,56] This is the method that is used to obtain the calculated profiles presented in Sec. V. Profiles of $\langle U\rangle/\Delta U$ and $\langle u_i u_j\rangle/\Delta U^2$ are used as indicators of when the numerical solution has achieved self-similarity: in the self-similar regime, these normalized profiles plotted versus η are independent of time (or independent of x for the boundary-layer algorithm).

C. Boundary conditions

Boundary conditions are implemented in a straightforward way. The incoming particles representing the nonturbulent fluid have no fluctuations in the idealization described in Sec. III E; all are at a uniform velocity corresponding to the irrotational free stream and all have $\Phi^*=0$ or $\Phi^*=1$.

For the plane mixing layer, we require that $U^*=U_L$ on the low-speed side and $U^*=U_H$ on the high-speed side. It is necessary in addition to specify a dividing streamline, that is, a location where $\langle V\rangle=0$. We take this to be at $\eta=0$. It is observed experimentally that in fact the mixing layer moves into the low-speed stream.[27–30] Rodi[46] points out that the correct third boundary condition is $U_H V_H + U_L V_L = 0$ (for a flow extending to infinity). However, it was found that calculated spreading rates and profiles of mean quantities were insensitive to the choice of the dividing streamline location, so the computationally simpler form of this boundary condition was adopted.

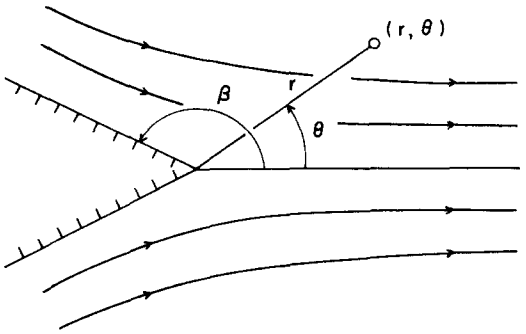

FIG. 7. The two-dimensional potential flow surrounding a plane jet.

Each of the other flows has a line or plane of symmetry, which fixes one of the boundary conditions. Another obvious boundary condition for the plane wake is that $U^*=U_E$ at the outer boundary. A third boundary condition is not required for the boundary-layer algorithm used for the plane wake, but for the two jets, V as well as U must be specified at the outer boundary of the computational domain, which is in the irrotational free stream. For the plane jet, the entrainment velocity V does not go to zero as $y\to\infty$, but rather it approaches a constant value at a fixed x.[57] The appropriate boundary conditions are derived by considering the incompressible, irrotational two-dimensional flow outside of the turbulent jet (Fig. 7). We let U_r and U_θ denote, respectively, the radial and tangential components of the velocity in polar cylindrical coordinates. It can be shown[58] that the velocity field in the free stream is given by

$$\begin{aligned} r^{1/2}U_r &= u^* \sin[(3\pi+\theta-\beta)/2], \\ r^{1/2}U_\theta &= u^* \cos[(3\pi+\theta-\beta)/2], \end{aligned} \quad (28)$$

where the angle β is defined in Fig. 7, and u^* is arbitrary. (Actually, Taylor [58] presents the solution only for the cases $\beta=\pi/2$ and $\beta=\pi$.) We choose $\beta=\pi$, corresponding to no wall at the jet exit and $u^*=0.05$; the latter choice is convenient as it gives $U_C\approx 1$ in the computations, but we emphasize that appropriately normalized (by $\Delta U=U_C$) quantities are independent of u^*.

For the axisymmetric jet, V goes to zero as $1/r'$, far from the axis of symmetry at a fixed x[57] (Fig. 4). In this case, we take $U_r=0$ and $U_\phi=-0.005/\phi$ on the computational boundary, where U_r and U_ϕ are the velocity components in the r and ϕ directions (Fig. 4). This corresponds to entrainment in the $-\phi$ direction with V proportional to $1/r'$, and again gives $U_C\approx 1$ in the computations.

V. RESULTS

Calculated profiles of the mean velocity, Reynolds stresses, and intermittency factor are compared with the experimental data selected in Sec. III. In all cases, the values of the model constants are those reported in Tables II and III. The abscissa of all plots is the similarity coordinate η appropriate to the flow, and all velocities are normalized by the velocity difference ΔU for the flow (Table I). Profiles are from a single time step (x step for the plane wake) of an $N \approx 100\,000$ Monte Carlo run after self-similarity is achieved.

A. Plane mixing layer

Calculated mean velocity profiles (Fig. 8) show generally good agreement with experimental data. Two of the models, SL and IL1, give high values on the low-speed side of the flow. The SL profile in particular is rather flat on the low-speed side. All models yield an intermittency factor profile that is too wide and shifted toward the low-speed stream; the PI model gives the widest γ profile and SL gives the narrowest.

The next four figures show the calculated Reynolds stress profiles (Figs. 9–12). These tend to be shifted toward the low-speed stream with respect to the experimental data; all models give Reynolds stress peaks near $\eta = 0$ while the experimental data indicate more asymmetric profiles with peaks on the high-speed side of the layer. The calculated shear stress profiles (Fig. 9) are good on the high-speed side, with peaks that match the experimental data of Patel,[28] but they extend too far into the low-speed stream. Profiles of the normal stresses (Figs. 10–12) show peak values that agree rather well with the data of Champagne *et al.*[27] Calculated profiles are narrowest for SL and widest for PI. The distribution of energy among the normal stresses is similar for all models. Only GL shows a significant difference between the peak $\langle v^2 \rangle$ and the peak $\langle w^2 \rangle$, with $\langle w^2 \rangle > \langle v^2 \rangle$, and IL1 has a higher peak $\langle u^2 \rangle$ than the other four models. From the available Reynolds stress data, it is not possible to conclude that one model performs better than another in this flow, but SL

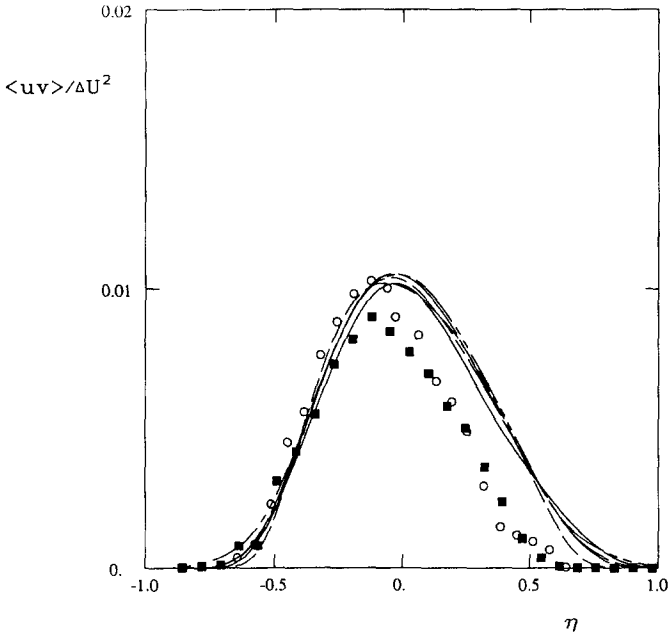

FIG. 9. Normalized profiles of the Reynolds shear stress $\langle uv \rangle$ versus the similarity variable η for the plane mixing layer. Lines are calculations, symbols are experimental data: —— GL; - - - - SL; — — IL1; — · — IL2; — -- — PI; ○ Patel[28]; ■ Wygnanski and Fiedler.[30]

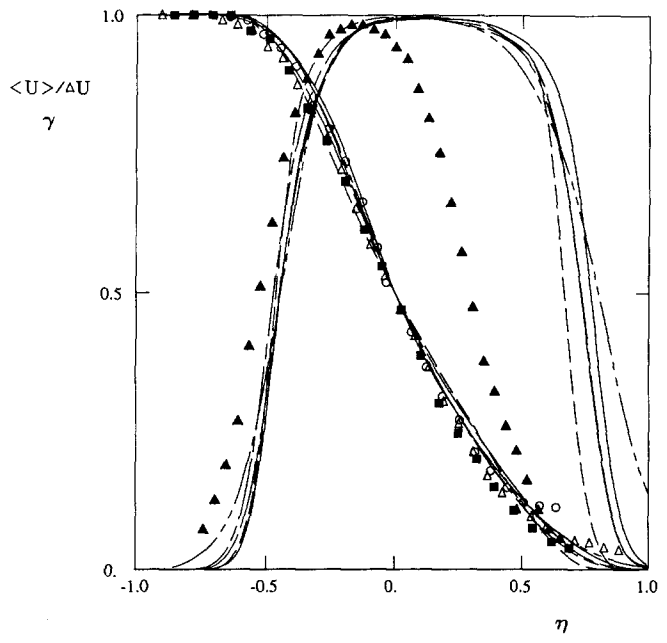

FIG. 8. Normalized profiles of the streamwise mean velocity and intermittency factor versus the similarity variable η for the plane mixing layer. Lines are calculations, symbols are experimental data: —— GL; - - - - SL; — — IL1; — · — IL2; — -- — PI; ○ $\langle U \rangle$, Patel[28]; ■ $\langle U \rangle$, Wygnanski and Fiedler[30]; △ $\langle U \rangle$, Champagne *et al.*[27]; ▲ γ, Wygnanski and Fiedler.[30]

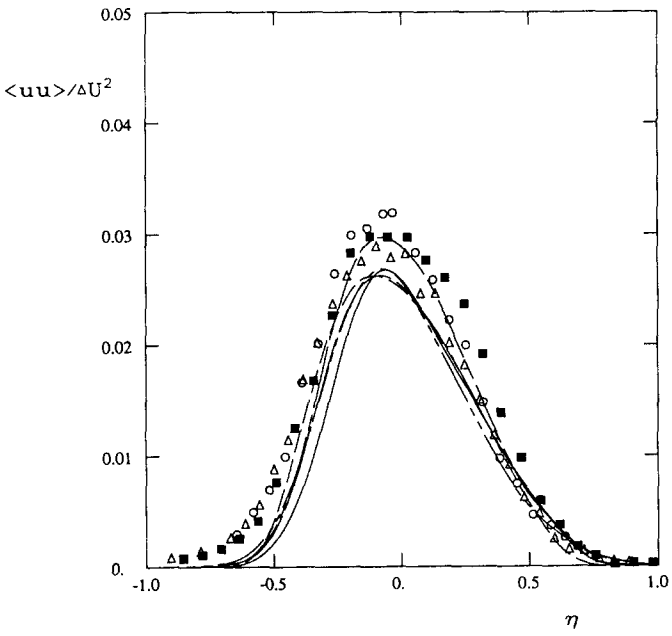

FIG. 10. Normalized profiles of the streamwise component of the Reynolds stress $\langle uu \rangle$ versus the similarity variable η for the plane mixing layer. Lines are the same as in Fig. 9; ○ Patel[28]; ■ Wygnanski and Fiedler[30]; △ Champagne *et al.*[27]

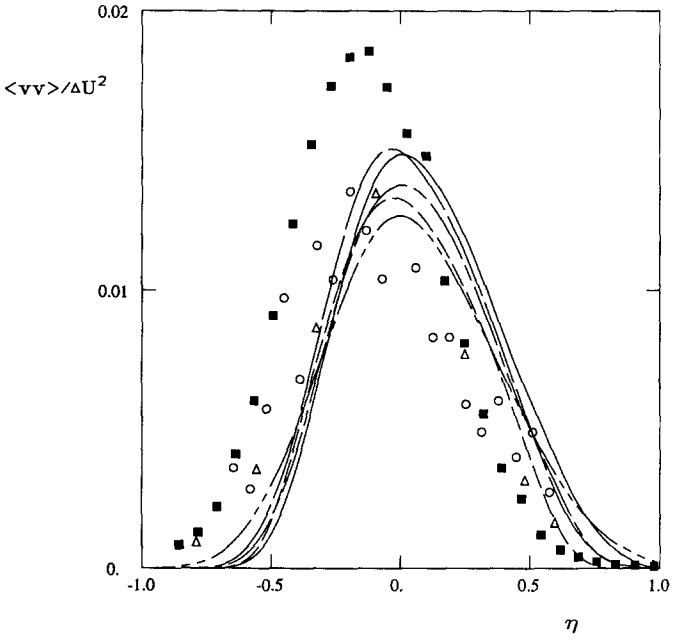

FIG. 11. Normalized profiles of the cross-stream component of the Reynolds stress $\langle vv \rangle$ versus the similarity variable η for the plane mixing layer. Lines and symbols are the same as in Fig. 10.

and IL1 appear to give poorer $\langle U \rangle$ profiles than the others (Fig. 8).

Calculated spreading rates are all somewhat low (Table IV), although the GL value is closer than the other four to the experimental value. At first sight, this seems to be inconsistent with the fact that the calculated peak of $\langle uv \rangle / \Delta U^2$ is in agreement with the data. However, the measure of spreading that has been adopted here (Table I) is sensitive to small changes in the $\langle U \rangle$ profile near the edges of the mixing layer.

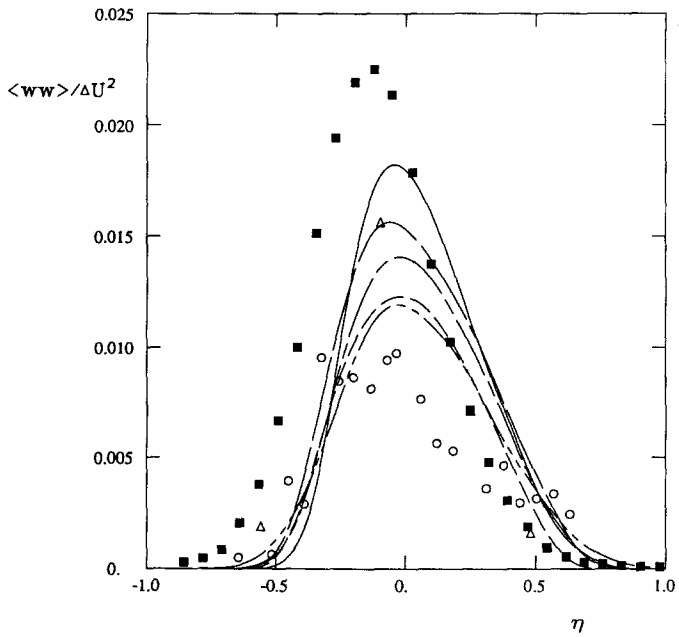

FIG. 12. Normalized profiles of the transverse component of the Reynolds stress $\langle ww \rangle$ versus the similarity variable η for the plane mixing layer. Lines and symbols are the same as in Fig. 10.

TABLE IV. Measured versus calculated spreading rates for four self-similar free shear flows.

		Spreading rates S				
Flow	Measured	GL	SL	IL1	IL2	PI
Plane mixing layer	0.18–0.19	0.150	0.130	0.130	0.125	0.130
Plane wake	0.098	0.078	0.095	0.074	0.073	0.093
Plane jet	0.100	0.096	0.100	0.095	0.095	0.099
Axisymmetric jet	0.086	0.084	0.083	0.078	0.086	0.085

It may be seen in Fig. 8 that there are discernible differences between the calculations and the experiments (as well as among the three sets of experimental data themselves and among the five models themselves) at the edges of the mixing layer. Both the experimental uncertainty and the effects of the intermittency modeling in the calculations are greatest near the edges of the flow.

B. Plane wake

For this flow, there is again general agreement between the calculated and measured mean velocity profiles (Fig. 13). The IL1 profile deviates from the experimental data near the plane of symmetry ($\eta = 0$), while GL shows the greatest difference at the outer edge. All five calculated intermittency factor profiles are reasonably close to the Fabris[33] data at the edge, but they fail to attain the value of unity at $\eta = 0$, peaking at a value of about 0.95. Here SL gives the narrowest turbulent region while GL and PI give the widest.

All models undershoot the peak shear stress reported by Townsend[32] (Fig. 14), although SL comes close. For this

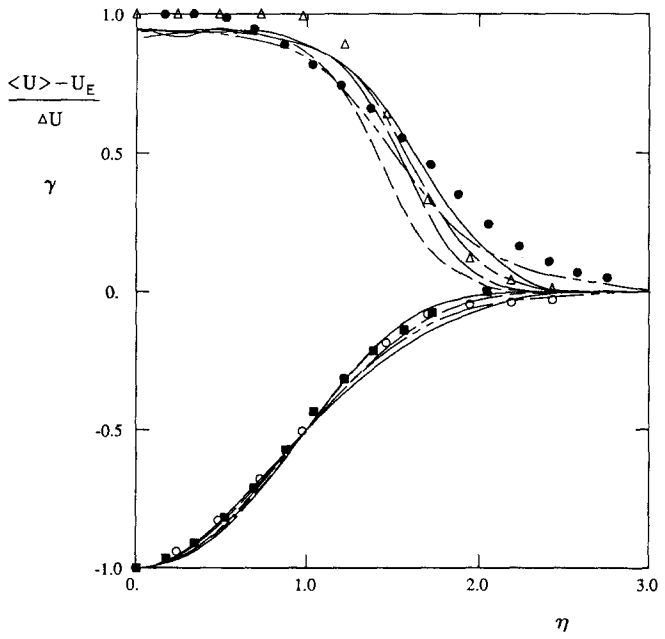

FIG. 13. Normalized profiles of the streamwise mean velocity and intermittency factor versus the similarity variable η for the plane wake. Lines are calculations, symbols are experimental data: —— GL; - - - - SL; — — IL1; — · — IL2; — · · — PI; ○ $\langle U \rangle$, Fabris[33]; ■ $\langle U \rangle$, Townsend[32]; △ γ, Fabris[33]; ● γ, Townsend.[32]

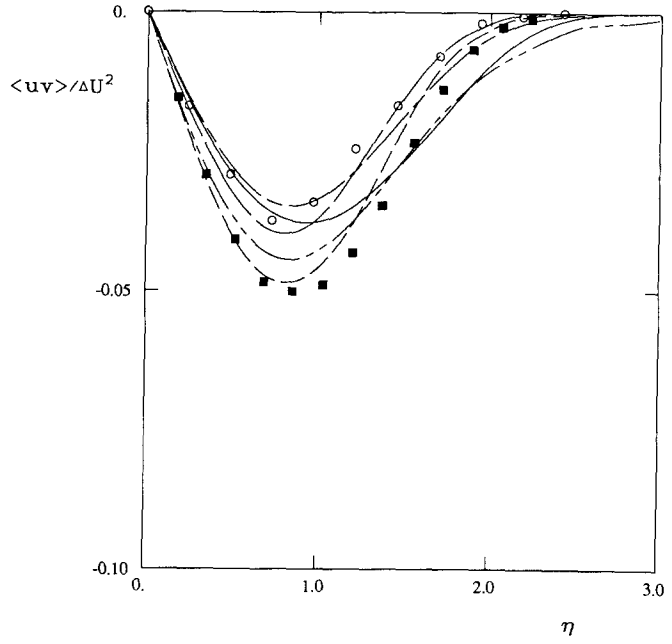

FIG. 14. Normalized profiles of the Reynolds shear stress $\langle uv \rangle$ versus the similarity variable η for the plane wake. Lines are calculations, symbols are experimental data: —— GL; - - - - SL; — — IL; — · — · IL2: — — — PI; ○ Fabris[33]; ■ Townsend.[32]

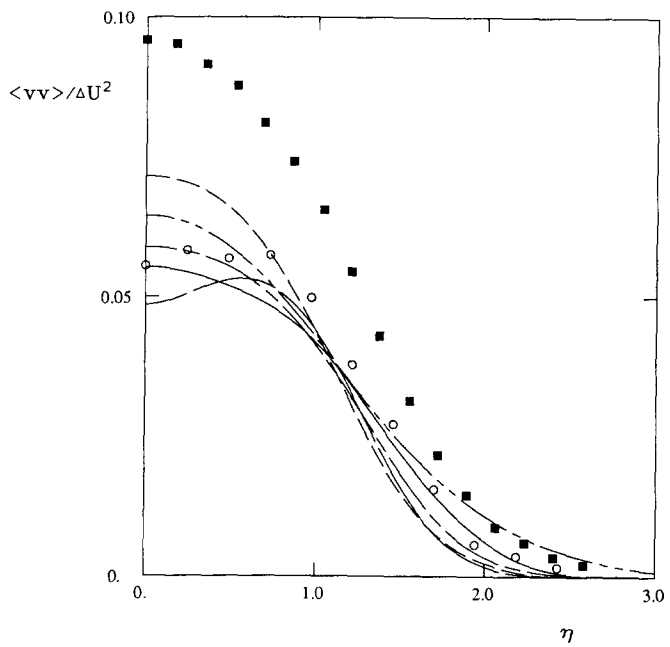

FIG. 16. Normalized profiles of the cross-stream component of the Reynolds stress $\langle vv \rangle$ versus the similarity variable η for the plane wake. Lines and symbols are the same as in Fig. 14.

flow, we were not able to chose ω^* in a way that matched the peak $\langle uv \rangle / \Delta U^2$; decreasing ω^* further causes the calculations to become unstable.

Figures 15–17 show that in all cases, the models tend to put too much energy into the streamwise component $\langle u^2 \rangle$ while $\langle v^2 \rangle$ and $\langle w^2 \rangle$ match the Fabris profiles fairly well. The overall energy levels are larger for the models with the higher $\langle uv \rangle$, as expected, and the distribution of energy among the three normal stresses is similar in all cases, with $\langle v^2 \rangle$ and $\langle w^2 \rangle$ peaks being nearly equal. All five exhibit a prominent off-axis peak in $\langle u^2 \rangle$, but only IL1 shows any significant off-axis peak in $\langle v^2 \rangle$ and $\langle w^2 \rangle$. It is the GL and PI profiles that extend furthest into the free stream, and SL and IL1 that drop off most rapidly at the outer edge of the wake.

With the exceptions of SL and PI, calculated spreading rates (Table IV) are low, consistent with the low calculated shear stresses.

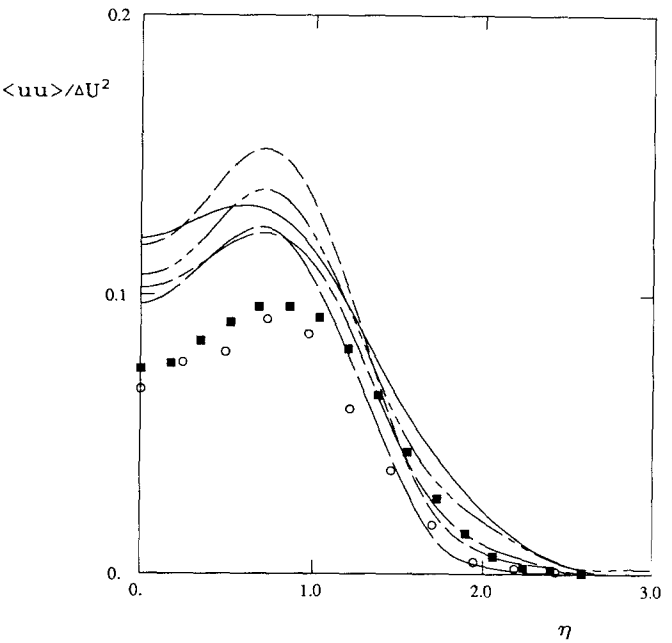

FIG. 15. Normalized profiles of the streamwise component of the Reynolds stress $\langle uu \rangle$ versus the similarity variable η for the plane wake. Lines and symbols are the same as in Fig. 14.

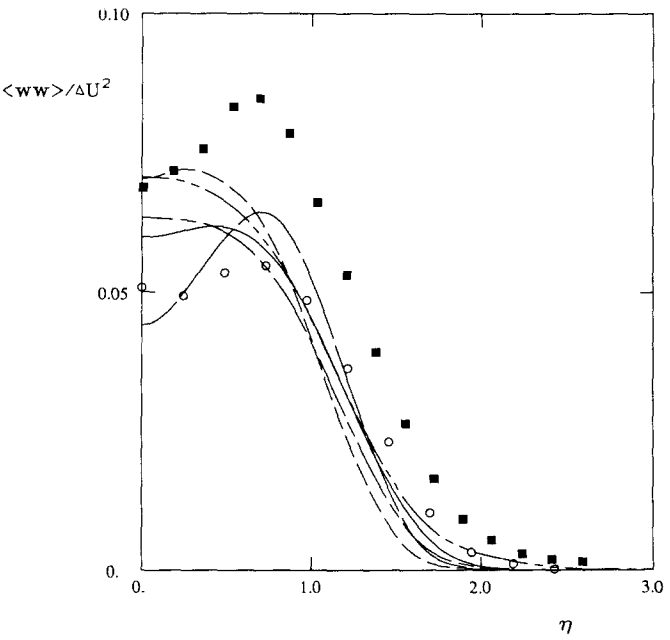

FIG. 17. Normalized profiles of the transverse component of the Reynolds stress $\langle ww \rangle$ versus the similarity variable η for the plane wake. Lines and symbols are the same as in Fig. 14.

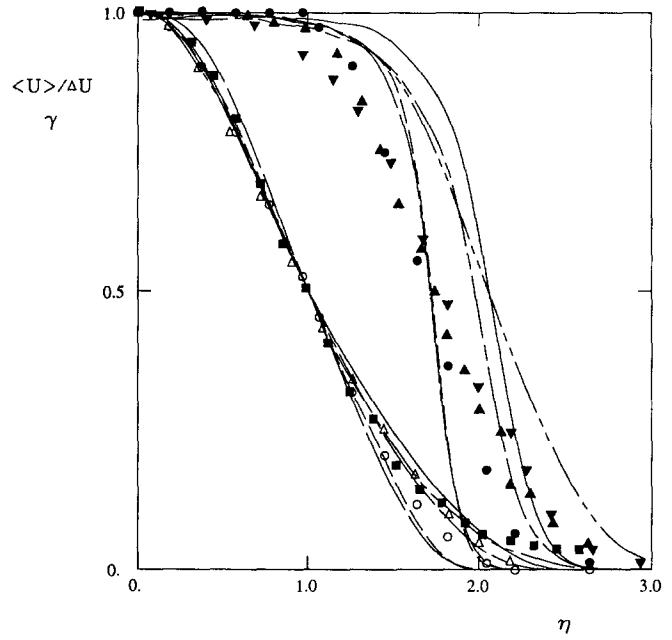

FIG. 18. Normalized profiles of the streamwise mean velocity and intermittency factor versus the similarity variable η for the plane jet. Lines are calculations, symbols are experimental data: —— GL; - - - - SL; — — IL1; — - —IL2; — -- — PI; ○ $\langle U \rangle$, Bradbury[40]; ■ $\langle U \rangle$, Gutmark and Wygnanski[41]; △ $\langle U \rangle$, Heskestad[36]; ● γ, Bradbury[40]; ▲ γ, Gutmark and Wygnanski[41]; ▼ γ, Heskestad.[36]

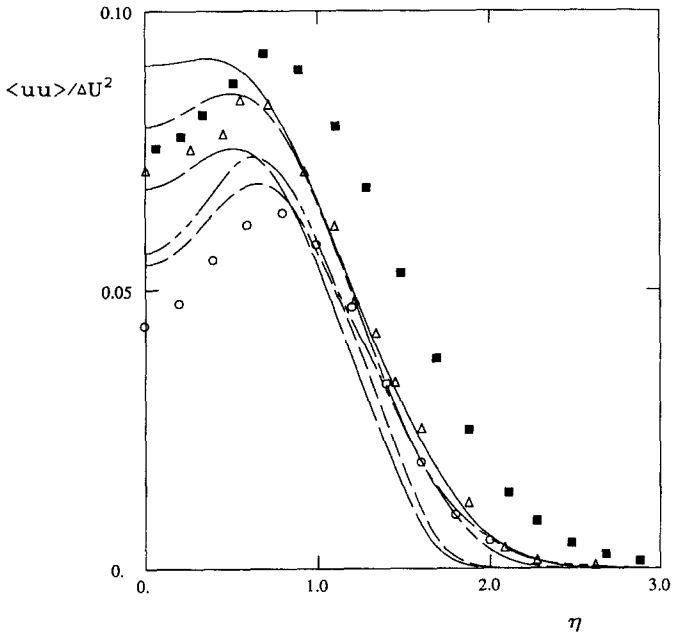

FIG. 20. Normalized profiles of the streamwise component of the Reynolds stress $\langle uu \rangle$ versus the similarity variable η for the plane jet. Lines and symbols are the same as in Fig. 19.

C. Plane jet

Results for the plane jet are given in Figs. 18–22. The mean velocity profiles (Fig. 18) for two of the models, SL and IL1, drop to zero too rapidly at the outer edge. The intermittency factor profiles for these two are too steep and imply a turbulent zone that is much narrower than the experimental data indicate. For GL and IL2, the intermittency factor profiles are still quite steep, but they go to zero closer to the η value indicated by the data. The PI profile parallels the experimental curve but extends further into the surrounding field. (If we had retained the value $C_g = 1.5$ in the conditional modeling of Sec. III E, the present PI calculations would be identical with those reported in Ref. 12, where the calculated intermittency factor profile for the

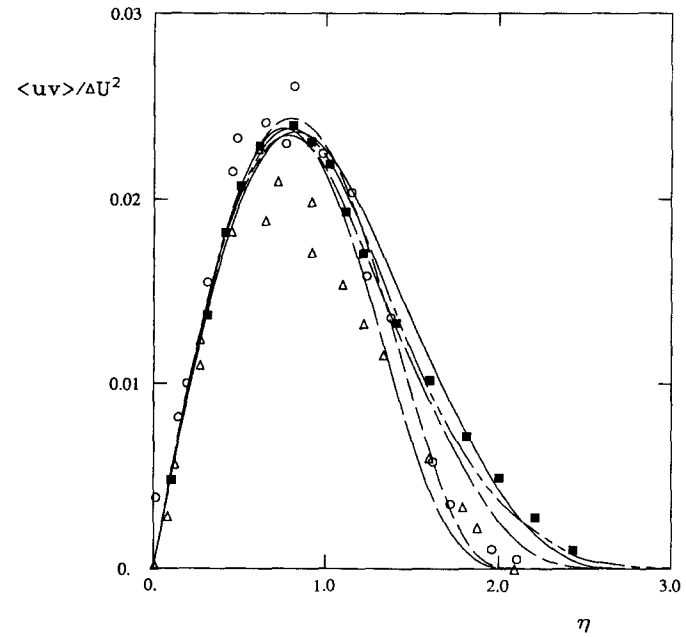

FIG. 19. Normalized profiles of the Reynolds shear stress $\langle uv \rangle$ versus the similarity variable η for the plane jet. Lines are calculations, symbols are experimental data: —— GL; - - - - SL; — — IL1; — - — IL2; — -- — PI; ○ Bradbury[40]; ■ Gutmark and Wygnanski[41]; △ Heskestad.[36]

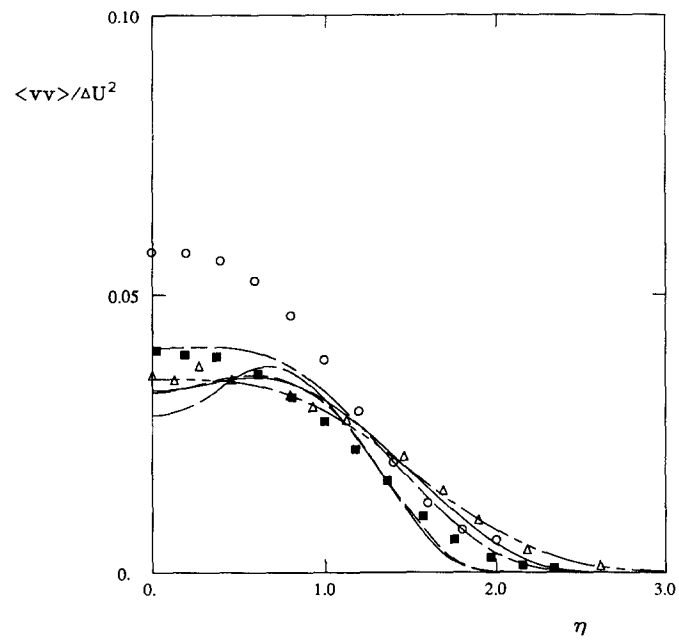

FIG. 21. Normalized profiles of the cross-stream component of the Reynolds stress $\langle vv \rangle$ versus the similarity variable η for the plane jet. Lines and symbols are the same as in Fig. 19.

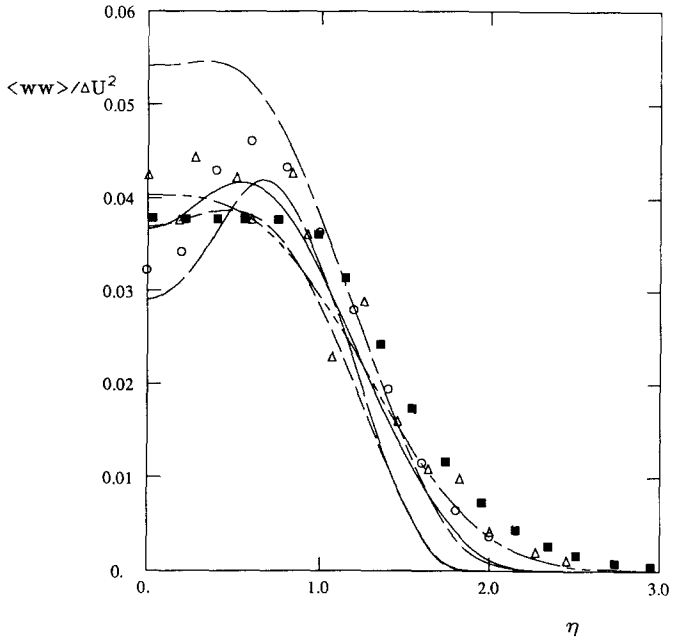

FIG. 22. Normalized profiles of the transverse component of the Reynolds stress $\langle ww \rangle$ versus the similarity variable η for the plane jet. Lines and symbols are the same as in Fig. 19.

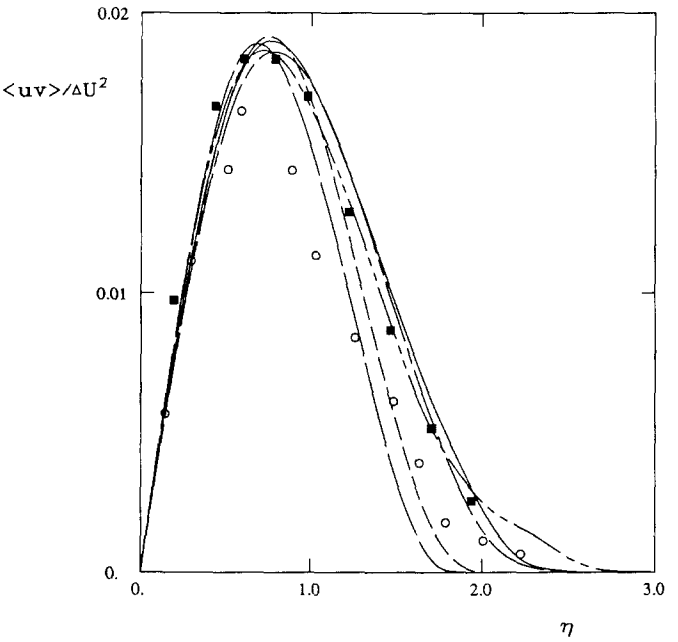

FIG. 24. Normalized profiles of the Reynolds shear stress $\langle uv \rangle$ versus the similarity variable η for the axisymmetric jet. Lines are calculations, symbols are experimental data: —— GL; - - - - SL; — — IL1; — · — IL2; — — — PI; ○ Wygnanski and Fiedler[45]; ■ Rodi.[46]

plane jet was in excellent agreement with the data.)

Shear stress profiles (Fig. 19) calculated by GL and PI agree remarkably well with the data of Gutmark and Wygnanski.[41] The IL2 profile tails off somewhat more rapidly and both SL and IL1 profiles are extremely steep on the outer side of the jet. These same features are evident in the normal stress profiles, Figs. 20–22. Here it may also be seen that all models give an off-axis peak in $\langle u^2 \rangle$ and IL1 gives the most prominent off-axis peaks in $\langle v^2 \rangle$ and $\langle w^2 \rangle$. GL and IL2 put more into $\langle u^2 \rangle$ than the other three models, the $\langle v^2 \rangle$ peaks are similar for all models, and only IL2 shows a peak $\langle w^2 \rangle$ that is noticeably higher than the others. All give a peak $\langle w^2 \rangle$ that is about 15%–25% greater than the $\langle v^2 \rangle$ peak. The GL model appears to yield the best overall agreement in

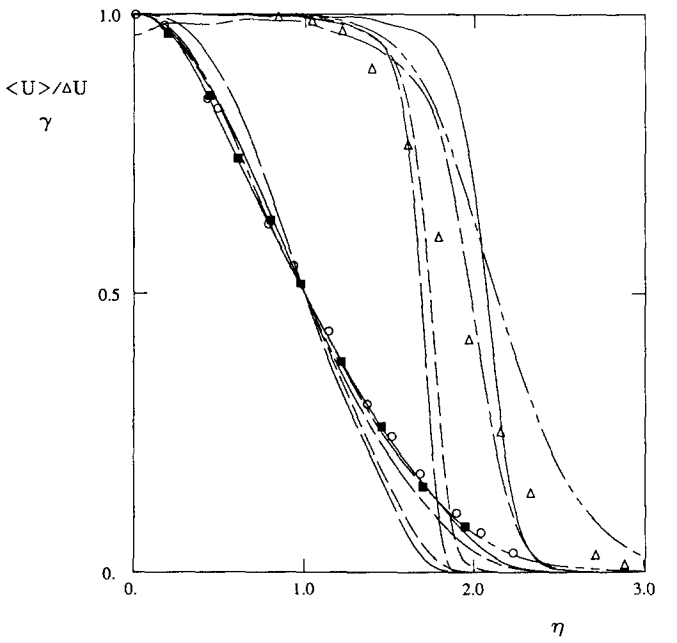

FIG. 23. Normalized profiles of the streamwise mean velocity and intermittency factor versus the similarity variable η for the axisymmetric jet. Lines are calculations, symbols are experimental data: —— GL; - - - - SL; — — IL1; — · — IL2; — — — PI; ○ $\langle U \rangle$, Wygnanski and Fiedler[45]; ■ $\langle U \rangle$, Rodi[46]; △ γ, Wygnanski and Fiedler.[45]

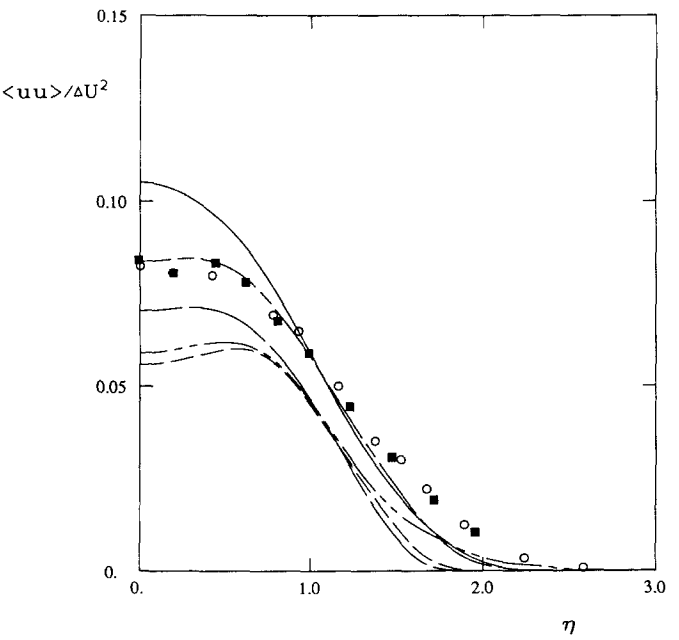

FIG. 25. Normalized profiles of the streamwise component of the Reynolds stress $\langle uu \rangle$ versus the similarity variable η for the axisymmetric jet. Lines and symbols are the same as in Fig. 24.

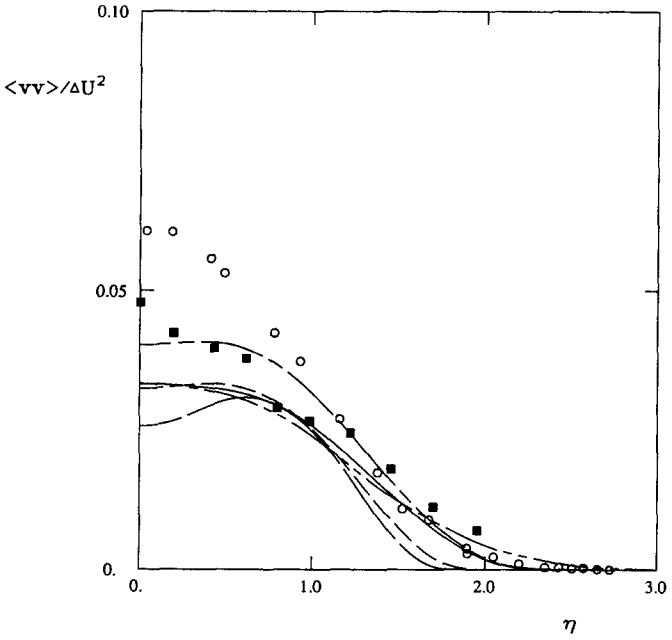

FIG. 26. Normalized profiles of the cross-stream component of the Reynolds stress $\langle vv \rangle$ versus the similarity variable η for the axisymmetric jet. Lines and symbols are the same as in Fig. 24.

the normal components with respect to the Gutmark and Wygnanski data, but IL2 is not far behind.

The calculated spreading rates (Table IV) vary from 0.095 to 0.100, in good agreement with the target value of 0.100.

D. Axisymmetric jet

The final flow considered is the axisymmetric jet. Most of the features observed in the calculated plane jet profiles

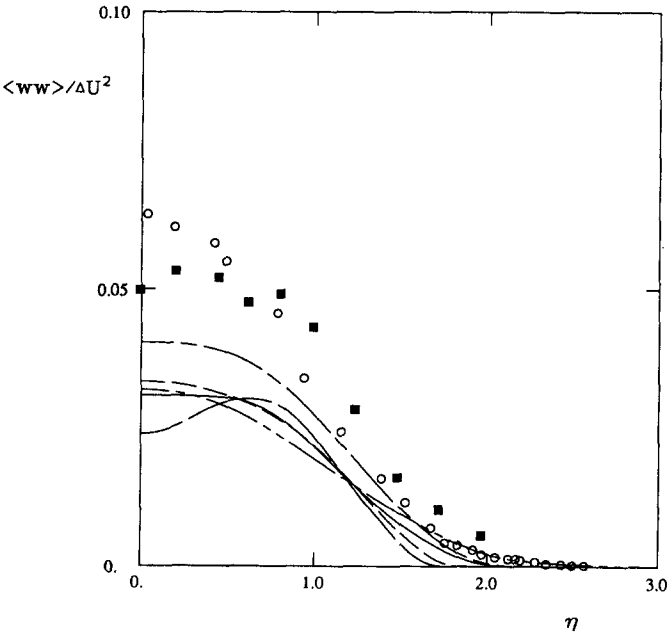

FIG. 27. Normalized profiles of the transverse component of the Reynolds stress $\langle ww \rangle$ versus the similarity variable η for the axisymmetric jet. Lines and symbols are the same as in Fig. 24.

are again evident here. The SL and IL1 mean velocity profiles again fall to zero too rapidly at the outer edge (Fig. 23). Here, the IL1 profile deviates noticeably from the data near the axis of symmetry as well. Trends in the calculated intermittency factor profiles are identical to those noted for the plane jet.

The calculated Reynolds stress profiles (Figs. 24–27) again show a tendency for PI to give the widest profiles and SL and IL1 the narrowest. The GL model again gives the highest $\langle u^2 \rangle$, while for $\langle v^2 \rangle$ and $\langle w^2 \rangle$, it is the IL2 profile that lies above the others. There are at most only moderate off-axis peaks in the calculated normal stresses, with the exception of the IL1 $\langle v^2 \rangle$ and $\langle w^2 \rangle$ profiles. For all five models, the peak values of $\langle v^2 \rangle$ and $\langle w^2 \rangle$ are nearly identical. The distribution of energy among the normal stresses appears to be best for IL2. GL puts too much into $\langle u^2 \rangle$ at the expense of $\langle v^2 \rangle$ and $\langle w^2 \rangle$, and the remaining three models appear to have too little energy overall.

The calculated spreading rates (Table IV) are all within a few percent of the measured value of 0.086, except IL1, which gives a spreading rate of just 0.078.

E. Summary

The overall level of agreement between calculated and measured profiles of the unconditional one-point statistics for the four flows is good for at least three of the models: GL, IL2, and PI. The deficiencies of the other two models are most evident in the jet flows, where the calculated mean velocity profiles show poor agreement with experimental data and the calculated Reynolds stress profiles fall off too rapidly at the outer edge. However, SL is the model that allows the measured spreading rate of the plane wake to be most closely approached. The calculated peak shear stress and spreading rates for the first three models are in agreement with experimental values for three of the four flows, the exception being the plane wake. Spreading rates for the four flows and five models are summarized in Table IV.

For these free shear flows at least, any of the GL, IL2, or PI models appears to be satisfactory. It should be realized from Table III that different specifications of ω^* are required for each model in a given flow. Thus, when these models are used together with a more general treatment of the turbulence scale (see Sec. VI), different results may be obtained. The ω^* values chosen for both GL and PI are very similar, while for IL2, somewhat lower values are called for. For the two models deemed inadequate in this study, SL and IL1, the required ω^* values are generally higher than for the other models.

Overall, the conditional modeling used here is found to be unsatisfactory. While it is possible to choose values for the three model constants C_g, C_m, and C_e to match the intermittency factor profile (and profiles of conditional mean velocities, which are not reported here) for either the plane wake or the two jets for a given velocity model, no values were found that give adequate results for all three symmetric flows; the values selected (Table II) represent a compromise. Moreover, there is no choice of the model constants that significantly improves the calculated intermittency factor profile for the plane mixing layer. It appears that a seri-

ous reexamination of the intermittency modeling is required to develop a model that performs equally well both in the symmetric flows and in the asymmetric mixing layer. This is discussed further in the next section.

Not surprisingly, the conditional models appear to work best in conjunction with the PI velocity model. The particle pair interactions allow a more gradual transition between the fully nonturbulent and fully turbulent regions than the Langevin-based models, leading to the steeper calculated γ profiles for the latter models. The fact the SL and IL1 do not work well in these flows while PI does is probably attributable to a combination of the velocity modeling plus the intermittency modeling; the use of different conditional modeling might change the conclusions of this study to some extent.

VI. CONCLUSIONS

A conditionally modeled joint pdf equation has been solved by a Monte Carlo method to calculate the one-point statistics of four self-similar free shear flows. This work extends the generalized Langevin model of Ref. 1 to inhomogeneous shear flows and tests the generality of the intermittency models developed in Ref. 12 by applying them to a broader class of flows. It also evaluates the performance of several simpler pdf models in free shear flows. Two of the simpler models are found to yield results comparable to those achieved with the more general model in these flows.

The principal conclusions are as follows. First, a set of model constants has been found for the generalized Langevin model that gives good results both in the homogeneous flows and in the self-similar free shear flows. This new set supercedes the values reported in Ref. 1 (see Table II). Second, the intermittency modeling is found to be inadequate, particularly for the asymmetric plane mixing layer. Some of the intermittency models developed by other workers[4,12,59–65] realized better agreement of the calculated intermittency factor profile with experimental data for the symmetric free shear flows than is reported here. However, the only reported profiles for the plane mixing layer are those of Libby[59] and Kollmann.[64] Libby's profile showed good agreement with experimental data, but this is achieved by using different values for the model constants on the low- and high-speed sides of the flow; the profile calculated by Kollmann looks remarkably similar to those calculated using the present models (Fig. 8).

While simpler classes of models[20,46,66,67] have shown mean velocity and Reynolds stress profiles as good as or better than those reported here for some flows, there is, to our knowledge, no second-order closure that does as well overall as the GL pdf model in both the homogeneous flows[1] and in the four free shear flows investigated in the present study. In all fairness, it should be pointed out that the second-order modeling studies generally include a modeled dissipation equation; the dissipation time scale was prescribed directly here.

In homogeneous turbulent flows, each of the five velocity models studied here reduces to a second-order closure, that is, the modeled moment equations are closed at the Reynolds stress level. In the pdf method, no additional modeling is then needed to treat inhomogeneous flows, while moment closures require a model for convective transport in physical space.[21] Thus while we have used pdf equations, the equivalent Reynolds stress model (plus a model for the third moments) could be used by others who feel more comfortable working with moment equations and finite-difference solution methods. This approach guarantees realizability of the Reynolds stresses[1] and can be expected to give good results for homogeneous flows and for free shear flows, at least.

One anomaly that has been found in applying the simpler classes of models to free shear flow is that the values of the model constants that give the proper spreading rate for the plane jet overpredict the spreading rate of the axisymmetric jet by about 40%.[46,67–70] This is usually attributed to the modeling of the dissipation equation. In fact, the dissipation equation is generally considered to be the weakest link in second-order closures.[21] The present study avoids this problem by specifying the turbulent time scale directly. This is appropriate for these thin free shear flows and is consistent with our philosophy of concentrating on the velocity modeling in this study, but it cannot be generalized to more complex flows, for example, statistically two- or three-dimensional flows with recirculation. A more general treatment of the dissipation is clearly called for to make the modeling truly predictive and more generally applicable.

As in second-order closures, a straightforward way to provide scale information in the pdf method is to use a standard modeled equation for the mean dissipation rate of turbulent kinetic energy ϵ, then to form the turbulent time scale according to Eq. (10). Recently, it has been found that a physically more appealing approach in the context of the pdf method and Lagrangian solution algorithm is to treat the dissipation as a random variable, and to model the dissipation rate following fluid particles in the flow.[16,71] That is, the pdf method can readily be extended to treat the joint pdf of velocity, composition, and dissipation. Because of the inclusion of dissipation, this joint pdf contains scale information and hence its modeled transport equation is closed. In addition, to take some account of internal intermittency,[72] the particle dissipation (rather than the mean ϵ) can be used in the random term of the Langevin models [Eq. (5)]. Good results are obtained using a model of this kind for the turbulence mixing layer.[16]

The particle dependent dissipation also allows intermittency to be treated in a straightforward way. The viscous dissipation associated with a particle provides a natural discriminator between turbulent and nonturbulent particles: the dissipation is zero for nonturbulent particles and positive for turbulent particles. Nonturbulent particles become turbulent by some stochastic process that effectively models the entrainment of nonturbulent fluid. All previous work on intermittency modeling[4,12,59–65] depends on the surrounding fluid being in a singular (irrotational) state and is not readily extended to multiple-time-scale fully turbulent flows—for example, a turbulent flow embedded in a surrounding turbulent field of different velocity and length scales. The particle dependent dissipation approach allows both intermittency and multiple scales to be treated in the same context.

It is expected that future work will concentrate on the

joint pdf of particle velocities, compositions, and dissipation, using the particle dependent dissipation both as a means of treating the turbulent time scale and as a means of modeling intermittency. Some of the recent studies of entrainment and mixing in the plane mixing layers[73–76] may help to shed more light on the intermittency modeling.

ACKNOWLEDGMENTS

This work was supported in part by Grant No. CPE-8212661 from the National Science Foundation, Engineering Energetics Program. Computations supporting this research were performed on the Cornell National Supercomputer Facility, which is supported in part by the National Science Foundation, New York State, and the IBM Corporation.

[1]D. C. Haworth and S. B. Pope, Phys. Fluids **29**, 387 (1986).
[2]S. B. Pope, Prog. Energy Combust. Sci. **11**, 119 (1985).
[3]S. B. Pope, Combust. Sci. Technol. **28**, 131 (1982).
[4]W. Kollmann and J. Janicka, Phys. Fluids **25**, 1755 (1982).
[5]D. C. Haworth and S. B. Pope, J. Comput. Phys., to be published.
[6]T. S. Lundgren, Phys. Fluids **10**, 969 (1967).
[7]T. S. Lundgren, Phys. Fluids **12**, 485 (1969).
[8]C. Dopazo and E. E. O'Brien, Acta Astronaut. **1**, 1239 (1974).
[9]J. Janicka, W. Kolbe, and W. Kollmann, J. Non-equilib. Thermodyn. **4**, 47 (1978).
[10]S. B. Pope, Phys. Fluids **24**, 588 (1981).
[11]S. B. Pope, in *Turbulent Shear Flows 3,* edited by L. J. S. Bradbury, F. Durst, B. E. Launder, F. W. Schmidt, and J. H. Whitelaw (Springer, Berlin, 1982), p. 113.
[12]S. B. Pope, AIAA J. **22**, 896 (1984).
[13]S. B. Pope and M. S. Anand, in *Twentieth Symposium (International) on Combustion* (The Combustion Institute, Pittsburgh, 1984), p. 403.
[14]M. S. Anand and S. B. Pope, in *Turbulent Shear Flows 4,* edited by L. J. S. Bradbury, F. Durst, B. E. Launder, F. W. Schmidt, and J. H. Whitelaw (Springer, Berlin, 1985), p. 46.
[15]D. C. Haworth and S. B. Pope, in *Fifth Symposium on Turbulent Shear Flows,* edited by L. J. S. Bradbury, F. Durst, B. E. Launder, F. W. Schmidt, and J. H. Whitelaw (Cornell University, Ithaca, NY, 1985), p. 3.13.
[16]S. B. Pope and D. C. Haworth, in *Turbulent Shear Flows 5,* edited by F. Durst, B. E. Launder, J. L. Lumley, F. W. Schmidt, and J. H. Whitelaw (Springer, Berlin, 1986), p. 44.
[17]S. B. Pope and S. M. Correa, in *Twenty-First Symposium (International) on Combustion* (The Combustion Institute, Pittsburgh, in press).
[18]S. B. Pope and W. K. Cheng, in Ref. 17.
[19]B. E. Launder and D. B. Spalding, *Mathematical Models of Turbulence* (Academic, New York, 1972).
[20]B. E. Launder, G. J. Reece, and W. Rodi, J. Fluid Mech. **68**, 537 (1975).
[21]J. L. Lumley, J. Appl. Mech. **50**, 1097 (1983).
[22]H. Tennekes and J. L. Lumley, *A First Course in Turbulence* (MIT, Cambridge, MA, 1972).
[23]W. Rodi, in *Studies in Convection,* edited by B. E. Launder (Academic, New York, 1975), Vol. 1, p. 79.
[24]A. A. Townsend, *The Structure of Turbulent Shear Flow* (Cambridge U. P., London, 1976).
[25]H.-H. Fernholtz, in *Turbulence,* edited by P. Bradshaw (Springer, Berlin, 1978), p. 45.
[26]A. E. Perry, *Hot-Wire Anemometry* (Clarendon, Oxford, 1982).
[27]F. H. Champagne, Y. H. Pao, and I. J. Wygnanski, J. Fluid Mech. **74**, 209 (1976).
[28]R. P. Patel, AIAA J. **11**, 67 (1973).
[29]R. P. Patel, Ph.D. thesis, McGill University, 1970.
[30]I. Wygnanski and H. E. Fiedler, J. Fluid Mech. **41**, 327 (1970).
[31]I. Wygnanski, F. Champagne, and B. Marasli, J. Fluid Mech. **168**, 31 (1986).
[32]A. A. Townsend, Aust. J. Sci. Res. Ser. A **2**, 451 (1949).
[33]G. Fabris, J. Fluid Mech. **94**, 673 (1979).
[34]R. M. Thomas, J. Fluid Mech. **57**, 549 (1973).
[35]A. Robins, Ph.D. thesis, University of London, 1971.
[36]G. Heskestad, J. Appl. Mech. **32**, 721 (1965).
[37]N. E. Kotsovinos, J. Fluid Mech. **77**, 305 (1976).
[38]P. Bradshaw, J. Fluid Mech. **80**, 795 (1977).
[39]M. K. Looney and J. J. Walsh, J. Fluid Mech. **147**, 397 (1984).
[40]L. J. S. Bradbury, J. Fluid Mech. **23**, 31 (1965).
[41]E. Gutmark and I. Wygnanski, J. Fluid Mech. **73**, 465 (1976).
[42]K. W. Everitt and A. G. Robins, J. Fluid Mech. **88**, 563 (1978).
[43]N. E. Kotsovinos, J. Fluid Mech. **87**, 55 (1978).
[44]W. Schneider, J. Fluid Mech. **154**, 91 (1985).
[45]I. Wygnanski and H. Fiedler, J. Fluid Mech. **38**, 577 (1969).
[46]W. Rodi, Ph.D. thesis, Imperial College, London, 1972.
[47]S. Corrsin and A. L. Kistler, N.A.C.A. Report No. 1244 (1955).
[48]C. G. Speziale, Geophys. Astrophys. Fluid Dyn. **23**, 69 (1983).
[49]V. G. Harris, J. A. H. Graham, and S. Corrisin, J. Fluid Mech. **81**, 657 (1977).
[50]S. Tavoularis and S. Corrsin, J. Fluid Mech. **104**, 311 (1981).
[51]J. C. Rotta, Z. Phys. **129**, 547 (1951).
[52]B. E. Launder (private communication).
[53]F. H. Champagne, V. G. Harris, and S. Corrsin, J. Fluid Mech. **41**, 81 (1970).
[54]R. L. Curl, AIChE J. **9**, 175 (1963).
[55]S. Corrsin, N.A.C.A. Report No. W-94, 1943.
[56]S. B. Pope and R. Gadh, submitted to SIAM J. Sci. Stat. Comput.
[57]H. Schlichting, *Boundary Layer Theory* (McGraw-Hill, New York, 1979).
[58]G. I. Taylor, J. Aerosol. Sci. **25**, 464 (1958).
[59]P. A. Libby, J. Fluid Mech. **68**, 273 (1975).
[60]P. A. Libby, Phys. Fluids **19**, 494 (1976).
[61]C. Dopazo, J. Fluid Mech. **81**, 433 (1977).
[62]R. Chevray and N. K. Tutu, J. Fluid Mech. **88**, 133 (1978).
[63]S. Byggstoyl and W. Kollmann, Int. J. Heat Mass Transfer **24**, 1811 (1981).
[64]W. Kollmann, AIAA Paper No. 83-0382 (1983).
[65]J. Janicka and W. Kollmann, in *Turbulent Shear Flows 4,* edited by L. J. S. Bradbury, F. Durst, B. E. Launder, F. W. Schmidt, and J. H. Whitelaw (Springer, Berlin, 1985), p. 73.
[66]D. S. A. Samaraweera, Ph.D. thesis, University of London, 1978.
[67]S. B. Pope, Philos. Trans. R. Soc. London Ser. A **291**, 529 (1979).
[68]B. E. Launder and D. B. Spalding, Comput. Meth. Appl. Mech. Eng. **3**, 269 (1974).
[69]S. B. Pope, AIAA J. **16**, 279 (1978).
[70]J. L. Lumley, in *Prediction Methods for Turbulent Flows,* edited by W. Kollmann (Hemisphere, New York, 1980), p. 1.
[71]D. C. Haworth and S. B. Pope, Bull. Am. Phys. Soc. **30**, 1694 (1985).
[72]A. S. Monin and A. M. Yaglom, *Statistical Fluid Mechanics: Mechanics of Turbulence* (MIT, Cambridge, MA, 1975), Vol. 2.
[73]P. E. Dimotakis and G. L. Brown, J. Fluid Mech. **78**, 535 (1976).
[74]M. G. Mungal and P. E. Dimotakis, J. Fluid Mech. **148**, 349 (1984).
[75]P. E. Dimotakis, AIAA Paper No. 84-0368, 1984.
[76]S. M. Masutani and C. T. Bowman, J. Fluid Mech. **172**, 93 (1986).